energies

MDPI

Article

A Preliminary Experimental and Numerical Analysis of a Novel Solar Dryer

Pio Francesco Muciaccia [1], Alessandra Nigro [1], Alessia Aquilanti [1], Sebastiano Tomassetti [1], Matteo Muccioli [2] and Giovanni Di Nicola [1,3,*]

[1] Department of Industrial Engineering and Mathematical Sciences, Marche Polytechnic University, Via Brecce Bianche 12, 60131 Ancona, Italy; p.f.muciaccia@pm.univpm.it (P.F.M.); a.nigro@univpm.it (A.N.); a.aquilanti@univpm.it (A.A.); s.tomassetti@univpm.it (S.T.)
[2] Studio MUMA, Via Eugenio Curiel 66 R, 47922 Rimini, Italy; matteo.muccioli@gmail.com
[3] Construction Technologies Institute, National Research Council (ITC-CNR), 35127 Padova, Italy
* Correspondence: g.dinicola@univpm.it

Abstract: In this study, a novel solar dryer is presented and analyzed experimentally and numerically. The proposed device is a small, passive, indirect solar dryer that works in an unconventional way. The product is mainly heated by irradiation from the walls of the drying chamber, while its moisture is removed by an airflow caused by natural convection. In addition, it is a low-cost solar dryer made of readily available materials and has a variable geometry that allows it to increase its thermal performance. Two types of experimental tests were conducted to analyze its performance. Thermal tests without load were carried out to assess the suitability of the drying chamber temperatures. Load tests with various masses and types of food were carried out to evaluate its drying performance. The results of the experimental tests demonstrated that the solar dryer achieved temperatures suitable for food drying and was able to dry the tested foods. Finally, a Computational Fluid Dynamics (CFD) model was developed to predict the performance of the proposed solar dryer. The validation of the numerical model with experimental data confirms their reliability in accurately predicting the temperatures within the dryer.

Keywords: solar energy; solar-energy drying systems; indirect solar dryer; natural convection solar dryer; CFD; solar load model; S2S radiation model

Citation: Muciaccia, P.F.; Nigro, A.; Aquilanti, A.; Tomassetti, S.; Muccioli, M.; Di Nicola, G. A Preliminary Experimental and Numerical Analysis of a Novel Solar Dryer. *Energies* **2024**, *17*, 6059. https://doi.org/10.3390/en17236059

Academic Editors: Mario Petrollese, Marco Francesconi and Elisa Sani

Received: 7 November 2024
Revised: 26 November 2024
Accepted: 27 November 2024
Published: 2 December 2024

1. Introduction

One of the main global challenges of our time is the need to ensure sufficient food resources for an ever-expanding world population. In this context, adopting environmentally friendly and affordable food drying strategies can significantly contribute to improving food safety and reducing post-harvest food losses.

The shelf life of many agricultural products is often significantly reduced by the high moisture content, which creates favorable conditions for the proliferation of bacteria and microorganisms [1]. This not only compromises food quality but also contributes to significant post-harvest losses. An effective solution to this issue is drying, a process that reduces the moisture level in products to safe levels, increasing shelf life and improving food management [2]. In addition, the final mass of the products is significantly reduced, facilitating both storage and transport [3]. The thermal drying process involves a simultaneous transfer of heat and mass: the heat transfer to the product causes the internal moisture to vaporize from its surface [1].

In the food sector, solar energy is considered a sustainable energy source for heating, cooking, drying, distillation, and water desalination. In many developing countries, the adoption of solar drying systems is a particularly advantageous and cost-effective solution, offering a sustainable alternative to methods requiring the use of traditional energy sources.

The drying of agricultural products by direct exposure to sunlight, known as open sun drying, involves exposing the crop to both sun and wind, usually lying on surfaces such as soil, mats, or trays. Although it is an ancient and widespread practice, it has several drawbacks that can lead to significant post-harvest losses and compromise product quality [2,4–6]. Some of the main issues are products' contamination due to exposure to the surrounding environment; degradation of the nutrients due to direct sunlight; irregular and long drying processes due to variable environmental conditions; risk of fermentation and mold development due to too slow drying; and the need for large areas to distribute the crops.

Several types of solar dryers have been developed to address many of these drawbacks and reduce dependence on traditional fuels. These systems are cost-effective and environmentally friendly solutions that ensure protected and controlled environments for drying foods. This significantly reduces the risk of environmental contamination and preserves food nutrients, improving preservation and quality of the products.

Among the different classifications of solar dryers [3–5], they can be divided into direct, indirect, and mixed-type dryers based on their exposure to solar radiation.

Direct solar dryers consist of a drying chamber with a transparent cover, usually made of glass or plastic, which allows the products to be directly exposed to solar radiation, limiting heat loss and protecting them from the environment. The absorbed radiation increases the temperature of the products and of the air inside the drying chamber. Colder and dry air enters through openings in the lower part, while warmer and moist air exits from the upper part, carrying away the products' moisture. These dryers are often inexpensive and easy to build. However, the product may suffer nutrient losses and product discoloration due to direct exposure to solar radiation, with limited temperature control and a relatively low drying rate, depending on the weather conditions.

Indirect solar dryers have a solar collector that captures heat and transfers it to an airflow, then sends it to a completely opaque drying chamber. The heated air, passing over the products, absorbs moisture and expels it through an outlet at the top of the chamber, thus avoiding direct exposure of the products to solar radiation. These dryers are more efficient than direct ones, as they avoid the issues related to direct sun exposure. However, their cost is generally higher than direct models [5].

Mixed solar dryers combine the features of direct and indirect dryers. Like indirect dryers, they heat the air through a dedicated system. However, they also include a transparent top in the drying chamber, similar to that of direct dryers, to optimize the absorption of solar radiation. This can speed up the drying process, reducing the time needed. However, as in the direct dryers, direct exposure to solar radiation can cause problems, such as nutrient losses and product discoloration [5].

Solar dryers are also classified into passive, active, and mixed, depending on the air movement within the device [3–5]. Passive dryers use natural convection for airflow: the sun-heated air spreads over the product surface, becomes moist due to evaporation, and then exits through an opening at the top of the dryer. Active dryers, on the other hand, use fans to have forced convection and transfer heat, making them particularly suitable for products with a high water content. Mixed dryers combine both modes. Some solar dryers are classified as hybrids, as they use another energy source to preheat the incoming air in addition to solar energy. These dryers accelerate the dehydration process compared to those using only solar energy due to higher temperatures and airflow rates.

Since the high potential of this technology, several studies analyzed the performance of different types of solar dryers, as proved by recent reviews on this topic [3,7]. For example, Jain et al. [8] numerically and experimentally studied a domestic direct passive multi-shelf solar dryer. More recently, some of these authors designed and evaluated an alternative solar dryer that relies on conduction rather than convection, achieving enhanced thermal performance [9]. Téllez et al. [10] analyzed direct and indirect solar technologies for drying stevia leaves. Haque et al. [11] described the design, development, and testing of an economical natural convection indirect solar dryer for domestic use in rural areas. Nabnean

and Nimnuan [12] analyzed the effectiveness of a forced convection direct solar dryer for drying bananas. A passive indirect solar dryer was studied by Lingayat et al. [13]. An indirect forced convection solar dryer was developed and evaluated by Umayal Sundari et al. [14]. Mugi and Chandramohan [15] studied the energy, exergy, and economic efficiency of an indirect solar dryer, comparing two operating modes: natural convection and forced convection, achieved through fans powered by photovoltaic panels. An innovative indirect solar dryer for drying chilies in the Western Himalayas was studied by Bhardwaj et al. [16], and Andharia et al. [17] experimentally and numerically analyzed the performance of a small-scale mixed-mode solar dryer integrated with sensible (black pebble stones) and latent (paraffin wax) heat storage materials. Shimpy et al. [18] reviewed various designs of solar dryers developed for domestic applications in rural and underdeveloped regions. More recently, Rulazi et al. [19] tested a novel passive solar dryer featuring a sensible thermal energy storage system, designed for regions with limited resources and intermittent solar availability.

It is important to note that the previously cited literature primarily focuses on studies conducted through experimental analysis. However, a complementary and advanced technique for enhancing the understanding and design of dryers is Computational Fluid Dynamics (CFD), which enables high-fidelity simulations of complex flows in complex geometries. It is today very widespread and applied to a wide range of fluid dynamics problems in many fields of industry and academia. The fast growth and the interesting experiences of CFD are mainly due to the increasing computational power, the high level of parallelization of the codes, and the use of advanced numerical models that allow a high accuracy level in a relatively moderate CPU time. Specifically, if applied to solar dryers, CFD can predict distributions of velocity and temperature, thus investigating the device performance and identifying the possible weaknesses of the system with the final aim to drive appropriate corrective actions for design improvement. In this regard, it should be noted that, even if the experimental investigation of a drying system is necessary to validate the CFD analysis, once the results of the numerical simulations have been validated, this tool provides a valid alternative to experimental analysis, since, especially in the phase of design optimization, it is more flexible and effective.

Several authors have used CFD in solar drying applications; see, for example, [20–22], only to name a few related to natural convection solar dryers, which is the type of dryer here proposed. One of the key points that emerges from the CFD studies already performed in this field is the need for a fine enough computational mesh and time step in order to predict transient three-dimensional calculations guaranteeing an appropriate level of accuracy of the numerical results. Furthermore, the effect due to the modelization of turbulence might be even of greater importance on the accuracy of the CFD prediction. The use of Detached Eddy Simulation (DES) or Large Eddy Simulation (LES) models [23,24] is expected to improve the accuracy of the numerical results with respect to the two-equation Reynolds Averaged Navier–Stokes (RANS) models [25], but their use is, in most cases, prohibitively expensive. In fact, the numerical modeling of solar dryers is a complex process that must take into account several aspects, e.g., the complexity of the geometry, fluid and solid properties, radiation models, heat conduction phenomenon, and unsteady turbulent flows. For the above reasons, the computational cost/accuracy trade-off must be accurately evaluated and often drives the decision to use approximate numerical models that have the ability, anyway, to predict the behavior of the most important physical quantities. This is especially true when the numerical models are used to improve the solar dryer design, since in this case it is important to quickly understand the pros and cons of several possible modifications. For an exhaustive review of recent advances and challenges in solar drying CFD simulations, the interested reader is referred to [3,26–28].

In this study, for the first time, the possibility of converting a solar cooker into an efficient solar dryer is evaluated. A small and simple solar dryer with natural convection, named the Newton Solar Dryer (NSD), based on a solar cooker, is presented. The prototype has a variable geometry to better concentrate solar radiation towards the drying chamber.

This chamber comprises two metal plates heated by solar radiation that, in turn, heat the loaded food mainly through irradiation. Instead, the airflow mainly removes the product moisture from the drying chamber. Consequently, the NSD can be categorized as an unconventional passive indirect solar dryer that does not require a blower or preheating of the airflow, unlike some dryers already available in the literature.

The dryer was tested experimentally to assess its drying performance and numerically to validate the computational models used in the CFD analysis, providing a starting point for future design optimization. In particular, the outdoor experimental campaign consisted of two types of tests: no-load thermal tests were carried out at different times of the year to see if the temperatures of the cooking chamber were suitable for food drying; load tests were carried out to evaluate its drying performance. In the load tests, the drying chamber was loaded with different masses and types of food.

The objectives that we aim to achieve in this study are the following:

- To present a new solar dryer that can be easily made with low-cost and readily available materials and that could be particularly useful in rural areas and developing countries where drying is mainly done by directly exposing foods to sunlight.
- To evaluate the performance of the solar dryer through comprehensive experimental testing.
- To validate its numerical modeling that will be used in future works, providing insights for further research and development.
- To contribute to the advancement of knowledge in the field of solar drying.

The paper is divided into the following sections. After the introduction, Section 2 describes the characteristics of the NSD and how the device works. The construction steps and materials selected for the prototype are explained in Section 3. Section 4 reports the experimental setup used to carry out the outdoor experimental campaign. Section 5 reports the results of the experimental study, divided between no-load thermal tests and food drying tests. Section 6 describes the CFD modeling used to perform the numerical analysis, its validation, and the analysis of the numerical results. The conclusions of the article are presented in Section 7.

2. Design and Optical Analysis

The solar dryer prototype presented in this paper, shown in Figures 1 and 2, is based on the design of the Newton solar cooker (NSC) proposed and characterized by Aquilanti et al. [29]. The NSC has the following main features:

- Ease of construction since it requires small and simple construction steps, making it assemblable even by an inexperienced operator;
- Low cost given the common materials chosen for its construction;
- Variable geometry for improving its thermal performance;
- Ease of transport, disassembly, and reassembly.

As clearly explained in the original study [29], the NSC consists of a prism-shaped cooking chamber having two panels of tempered glass on the sides and a wooden base on which a layer of insulating cork and a steel plate were placed. The device is equipped with two rotating support structures for the mirrors placed at the sides of the cooking chamber. By optimizing the inclination angles of the mirrors with respect to the sun's elevation, it is possible to maximize the amount of solar radiation concentrated on the cooking chamber. The results of the experimental campaign reported in [29] showed that the device was able to reach medium-high temperatures in a short time and with good efficiency. Furthermore, given the device's strengths, such as low cost and ease of implementation and use, it is considered suitable for developing countries, where it is seen as an environmentally friendly and healthy alternative to traditional cooking systems. For these reasons, it was decided to develop a new prototype suitable for food drying, starting from the simple design of the NSC with limited modifications. This resulted in the Newton Solar Dryer (NSD).

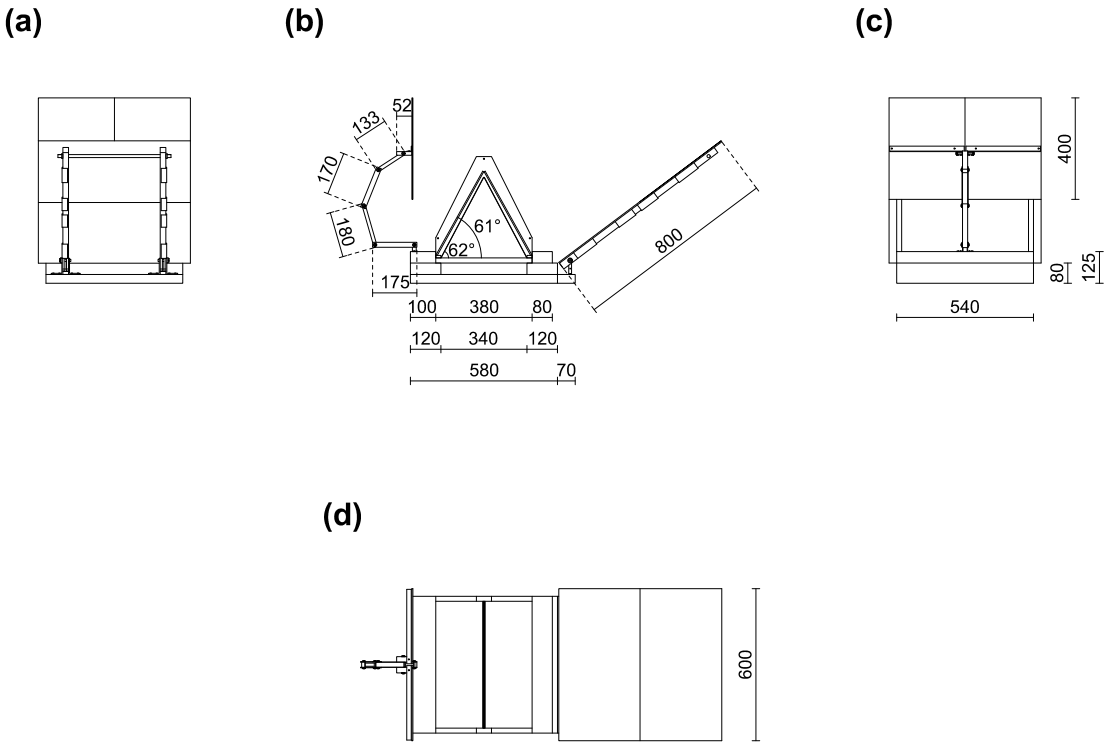

Figure 1. Newton Solar Dryer views (dimensions in mm): (**a**) left side view, (**b**) lateral view, (**c**) right side view, (**d**) top view.

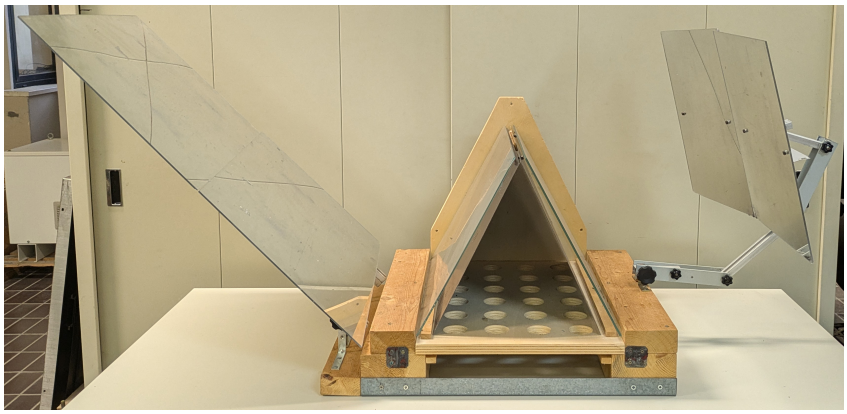

Figure 2. Photo of the Newton Solar Dryer.

The initial step in designing the new prototype was to define the operating requirements that a dryer must meet compared to a classic solar oven. The main difference between the two devices lies in the temperatures they are required to reach within their chambers: solar ovens need to reach the highest possible temperatures to speed up the cooking process; on the other hand, solar dryers need to reach and maintain temperatures in the range between 40 and 60 °C for a relatively long period. This also implies that the usage times of the two devices are different: cooking in solar ovens should take a short time, whereas, in the case of dryers, the required temperature should be maintained for a long time to ensure a complete drying (generally between 6 to 8 h, depending on the food inside the drying chamber). A further difference is the need for a constant airflow through the drying chamber: the dryer must ensure that the moisture removed from food is removed from the chamber through an airflow.

Considering the requirements just described and trying to make as few changes as possible to the NSC design, the version of the NSD prototype tested in this study was obtained after preliminary outdoor experimental tests. Figure 3 compares the two devices,

i.e., the NSC and NSD, with their main parts highlighted. From Figure 3, it can be seen that the dryer consists of a self-supporting wooden structure on which a perforated plate is placed to allow air to enter the device's drying chamber. In addition to the self-supporting wooden base, the drying chamber comprises two black steel plates, two extra-clear glass panels, and two side doors made of wood. It is worth noting that a gap was left on the top to ensure the airflow outlet from the drying chamber by spacing the steel plates and glass panes. Two metal arms are attached to the base, one on each side, to hold the mirrors of the device in place.

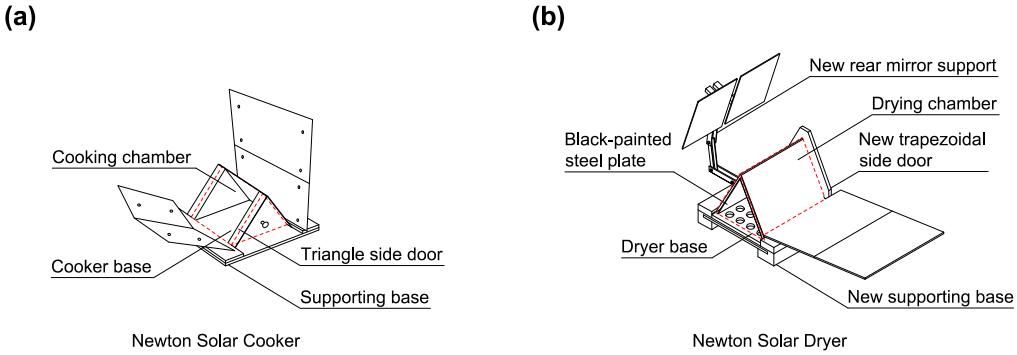

Figure 3. Comparison between NSC (**a**) and NSD (**b**). The cooking and drying chambers of the NSC and NSD, respectively, are highlighted with red dotted lines.

Figure 4 shows the working scheme of the NSD. The solar radiation (direct and reflected by the mirrors) heats up the two metal plates after passing through the glass panels. Since the greenhouse effect of the glass panels, the plates transfer the majority of heat to the contents of the chamber through irradiation. Air at ambient temperature enters the drying chamber in the lower part of the device and flows out from the upper part after heating up and absorbing the food moisture because of the chimney effect. The proposed device can be classified as a passive indirect dryer. However, it is unconventional since the product is mainly heated by radiation from the metal plates and only partially by the airflow. It is evident from Figure 4 that, like the NSC, the NSD has a variable geometry. By changing the angles of the mirrors' inclination with respect to the horizontal plane, the amount of radiation incident on the metal plates changes.

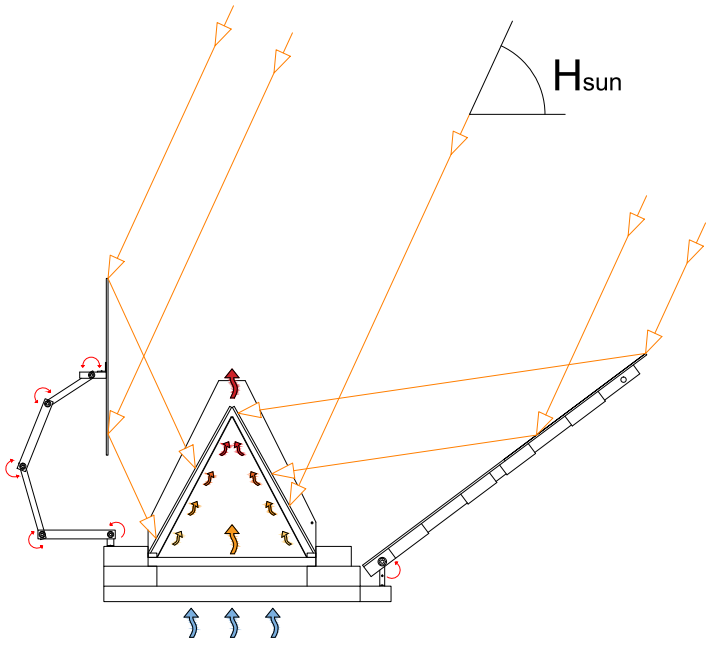

Figure 4. Working schema of the Newton Solar Dryer.

3. Manufacture and Assembly

The realization steps of the NSD are as follows: (1) construction of the supporting base; (2) assembly of drying chamber; (3) construction of side doors; (4) construction and assembly of mirrors. The details of each construction step are reported below.

3.1. Construction of the Supporting Base

Two 540 × 120 × 80 mm and two 540 × 100 × 40 mm blocks of glued laminated timber were coupled to obtain the supports for the dryer base. In particular, blocks with a larger cross-section were attached to the blocks with a smaller cross-section with screws and metal plates, as shown in Figure 5. This resulted in two overall L-shaped blocks used as supports for the dryer base. The base consists of a multilayer poplar panel with dimensions of 540 × 380 × 20 mm. To allow the airflow from the outside to the drying chamber, 24 holes with a diameter of 43 mm were drilled and arranged as shown in Figure 5. Two wooden laths of size 480 × 20 × 10 mm were placed on the drilled base in the proximity of each block.

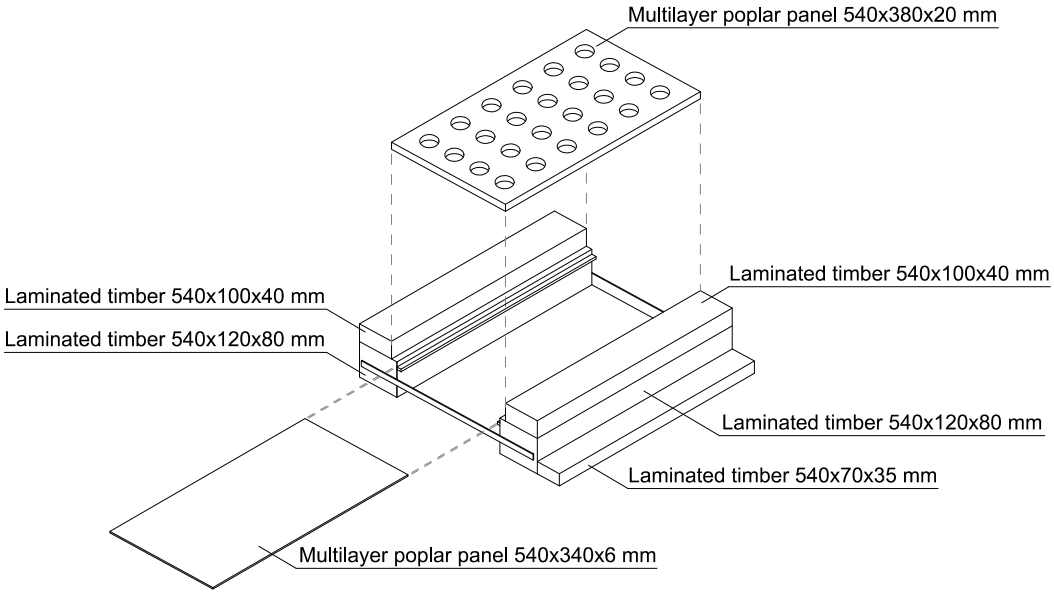

Figure 5. Details of the NSD base.

To ensure the stability of the dryer base, two steel bars (each 580 mm long) were used to hold the two blocks of the base at a distance of 340 mm. In addition, a 540 × 70 × 35 mm block of laminated wood was attached, also with screws, to one of the two previously assembled blocks to support the front mirror support arm.

The supporting structure is also equipped with a slot for inserting a multilayer poplar panel 6 mm thick and 540 × 340 mm in size. This panel regulates the air flowing in the drying chamber during the use of the device. The panel is slid on two rails consisting of two wooden strips of section 540 × 20 × 10 mm fixed to the structure with screws. The panel slides under the dryer base, closing the holes to reduce or stop the airflow.

3.2. Assembly of Drying Chamber

Two black-painted steel plates of size 480 × 380 mm and thickness of 2 mm were placed directly on the two 480 × 20 × 10 mm wooden laths of the perforated base, forming angles of about 60° with the base. The two sheets were held in place by spacers placed on top that provided an operator-variable gap to allow the outlet of hot and moist airflow.

Two extra-clear tempered glass plates of size 480 × 380 mm and thickness of 4 mm were placed directly on the wooden laths at the two blocks, again forming angles of about 60°. Specific spacers also hold in place the two glass plates, ensuring an air gap between them and the plates.

3.3. Construction of Side Doors

Two trapezoidal side doors were manufactured from a 20 mm thick poplar plywood panel to close the drying chamber sides. Figure 6 shows the chosen geometry and dimensions of the door. To ensure a better closure of the drying chamber, a tensioning system was used to hold in place and ensure better adhesion of the side doors to the glass and steel plates. To quickly open or close the drying chamber, ropes were passed through three holes drilled in both doors. At the ends of the three ropes, spring-loaded plastic cord clips were inserted: tensioning of the ropes ensures that the doors adhere to the drying chamber, and releasing them instead allows it to be opened. With this system, it is also possible to open the drying chamber from both sides and better control the internal temperatures.

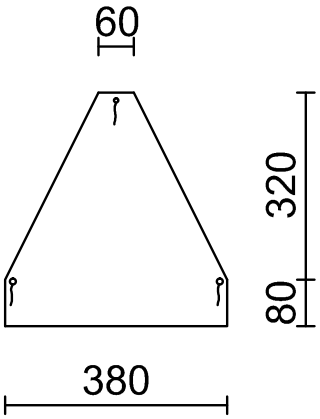

Figure 6. Side door of the NSD (dimensions in mm).

3.4. Construction and Assembly of Mirrors

The following mirrors made from polymethylmethacrylate (PMMA) sheets were used: two surfaces of 600 × 400 mm for the front mirror arranged contiguously in the same plane and two surfaces of 300 × 400 mm for the rear mirrors in a V-shaped configuration. Two steel hollow square profile bars with a cross-sectional area of 20 × 20 mm and a length of 650 mm were used to make the support arms for the front mirrors. The two metal bars were fastened and anchored to the 540 × 70 × 35 mm laminated wood block connected to the supporting structure of the solar dryer by angle brackets. The angle brackets were attached to the bars with a self-locking system to allow the whole support system to change the angle for proper sun tracking.

Eight aluminum C-profile pieces of 100 mm each were used to attach the front mirror to the support arms.

The rear mirror support consists of a five-hinge bar system as shown in Figure 4. The system is attached to the support structure by angle brackets. Two L-shaped metal profiles of length 300 mm were attached through two hinges to the last bar of the support. The two rear mirrors were attached to the L-shaped metal profiles using screws.

4. Experimental Setup and Test

Details about the experimental setup and tests are reported below.

4.1. Experimental Setup

Figure 7 shows the experimental setup used to carry out the experimental campaign. During the outdoor tests, the device was placed on a laboratory cart with wheels to facilitate sun orientation by the operator.

The quantities recorded during the tests were the temperatures inside the drying chamber (T_{Internal} in Figure 7), the temperatures of the black metal plates at the front and back (T_{Plates} in Figure 7), the temperatures of the glass panes (T_{Glass} in Figure 7), the air inlet temperatures inside the drying chamber measured at the base of the device ($T_{\text{Air\_inlet}}$

in Figure 7), the temperature of the air leaving the drying chamber (T_{Air_outlet} in Figure 7), the ambient temperature (T_{amb}), and the direct normal solar irradiance (G_{bn}).

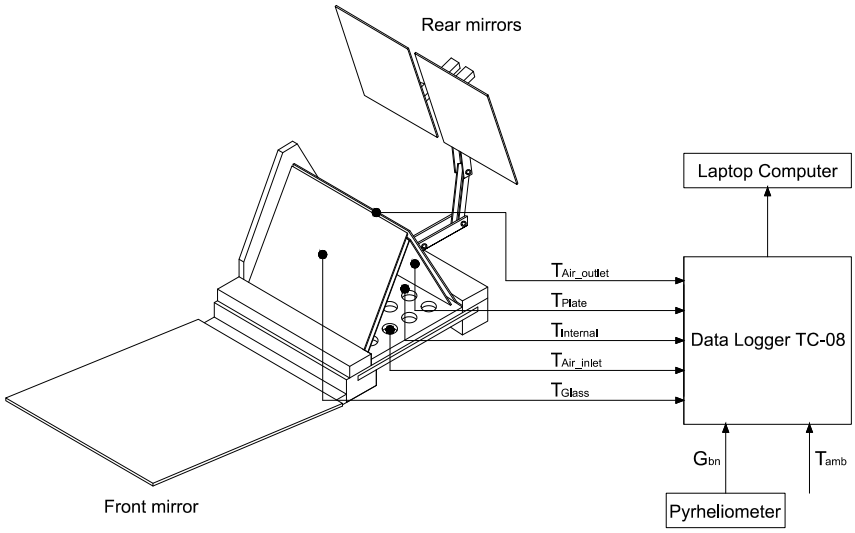

Figure 7. Experimental setup. T_{Air_outlet}: outlet air temperature from the drying chamber; T_{Plate}: metal plate temperature; $T_{Internal}$: air temperature inside the drying chamber; T_{Air_inlet}: inlet air temperature from the ambient; T_{Glass}: glass temperature; T_{amb}: ambient temperature; G_{bn}: direct normal irradiance.

The sensors used to record temperatures were T-type thermocouples with an uncertainty of $\pm 1\,^{\circ}C$. As shown in Figure 8, wooden frames were made to support the thermocouples in order to record the temperature gradient inside the drying chamber and on the main parts of the device. A high-temperature adhesive tape was used to hold the thermocouples in place on the structure throughout the individual tests, shielding the sensors from direct exposure to the sun. The thermocouple junction for recording the ambient temperature was, in turn, positioned in a shaded region to avoid the influence of direct exposure to the sun.

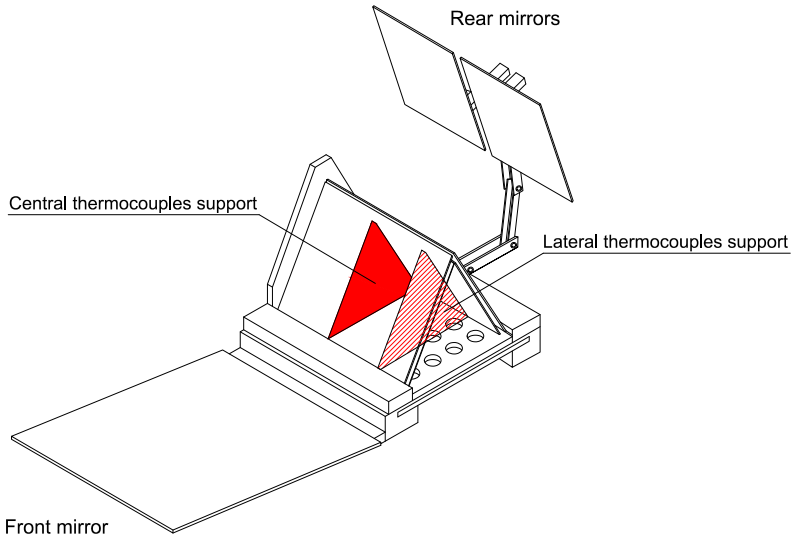

Figure 8. Scheme of the wooden structures for thermocouple supports. The lateral structure is placed at a distance of 120 mm from the central structure.

The positions of the thermocouples inside the drying chamber, on the metallic plates, and on the glass panes, together with those of the air entering and leaving the drying chamber, will be shown in detail for each individual test in the following sections.

An Epply NIP pyreliometer (normal incidence pyrheliometer) with a one-second response and linearity of ±0.5% in the range of 0 to 1400 W/m^2 was used to measure normal direct solar irradiance (G_{bn}). The thermocouple and pyreliometer signals were recorded by three Pico Technology TC-08 dataloggers with eight input channels each and sent to a computer.

Figure 9 shows the average environmental conditions referring to the time slot of the tests. While the values of the direct normal solar irradiance and ambient temperature were measured in the test site (latitude 43.5871° N, longitude 13.5149° E), the wind speed and air humidity were recorded in a location near the testing area (latitude 43.6098° N, longitude 13.5105° E). In particular, these data were collected from the Marche Region—Civil Protection Service website [30].

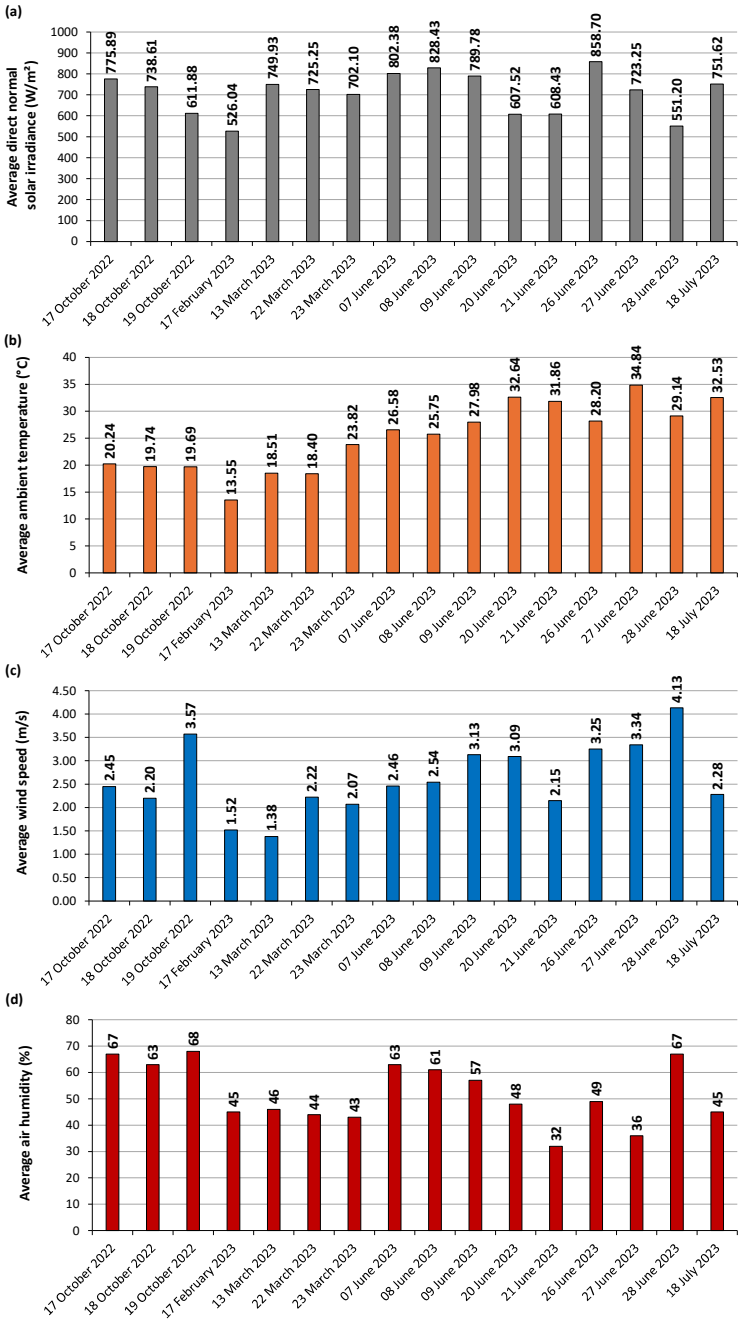

Figure 9. Average environmental conditions during the tests: (**a**) direct normal solar irradiance, (**b**) ambient temperature, (**c**) wind speed, and (**d**) air humidity.

4.2. Experimental Tests

The experimental campaign was carried out in September and October 2022 and February, March, June, and July 2023 on the roof of the Department of Industrial Engineering and Mathematical Sciences of the Università Politecnica delle Marche in Ancona, Italy (latitude 43.5871° N, longitude 13.5149° E). The device was tested avoiding shaded areas in the test area. During the tests, the operator aligned the device every 15 min in the sun's direction and simultaneously rotated the mirrors to maximize the amount of solar radiation concentrated on the drying chamber. The experimental campaign consisted of two different types of tests:

- Thermal tests of the unloaded device in which thermocouples were used to record the temperatures inside the drying chamber, the temperatures of the two black metal plates and the two extra-clear glass panels, and the temperatures of the air entering and leaving the drying chamber.
- Drying tests in which the drying chamber was loaded with different masses of foods.

5. Experimental Results

This section reports the results obtained from thermal and drying tests.

5.1. Thermal Tests

This section reports the outdoor experimental tests performed by measuring different temperatures of the dryer elements using three different configurations for the location of the thermocouples.

5.1.1. First Configuration

The test was conducted on 17 February 2023 using the device equipped with the front and rear mirrors. Figure 10 shows the arrangement of thermocouples in this test:

(a) Five thermocouples were attached to a wooden support placed in the central area of the drying chamber to record the internal temperatures (T_{I1}, T_{I2}, T_{I3}, T_{I4}, and T_{I5}).
(b) In the lateral area of the drying chamber (12 cm from the central support), five thermocouples were fixed to a wooden support inside the chamber to record the internal temperatures laterally (T_{I6}, T_{I7}, T_{I8}, T_{I9}, and T_{I10}).
(c) Four thermocouples were fixed on the rear metal plate (T_{P1}, T_{P2}, T_{P3}, and T_{P7}).
(d) Four on the front metal plate (T_{P4}, T_{P5}, T_{P6}, and T_{P8}).

The test started at 10:24 and ended at 14:20, local time. The average normal direct solar irradiance was about 526 W/m^2, while the average ambient temperature was about 13 °C.

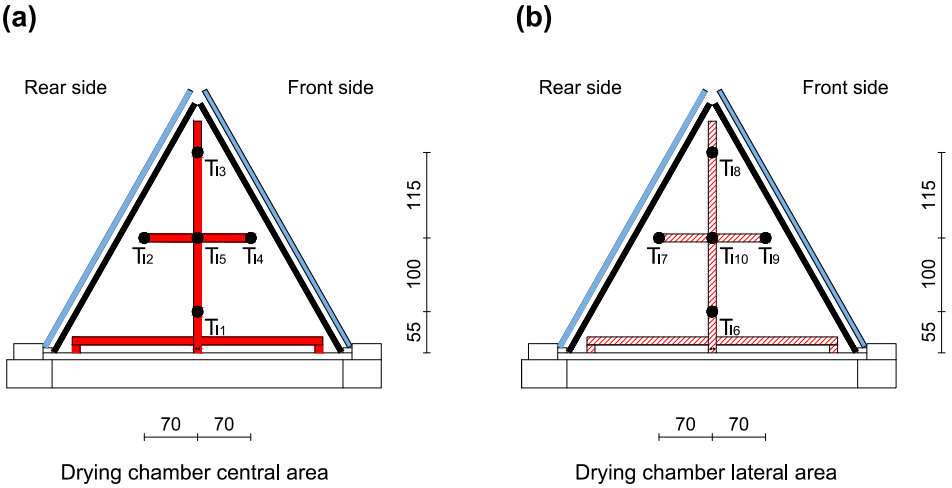

Figure 10. *Cont.*

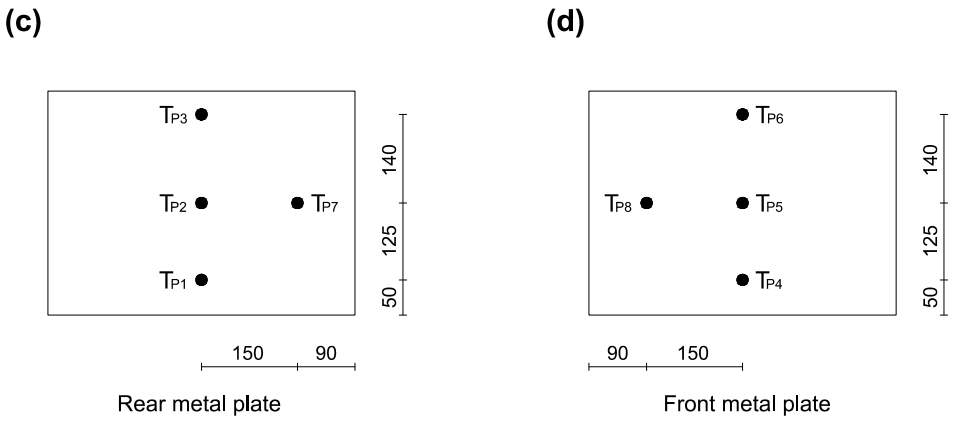

Figure 10. Position of the thermocouples for the 17 February 2023 test: (**a**) in the central area of the drying chamber; (**b**) in the lateral area of the drying chamber; (**c**) on the rear metal plate; (**d**) on the front metal plate. The dimensions are in mm. The thermocouple supports and the glass plates are highlighted in red and blue, respectively.

Table 1 shows the minimum, average, and maximum values of each temperature recorded during the test. The results show that the device, with the exclusion of the lower part of the drying chamber, is able to maintain internal temperatures suitable for drying food (above 35–40 °C and below 70 °C). Therefore, the device is suitable for food drying even when external conditions are not favorable: ambient temperature below 14 °C and average solar irradiance below 550 W/m^2.

Table 1. Temperatures recorded on the thermal test of 17 February 2023 using the first configuration of the thermocouples.

		17 February 2023 $T_{amb,av}$ = 13.55 °C and $G_{bn,av}$ = 526.04 W/m^2		
Recorded Temperatures	**Items**	T_{min} (°C)	T_{av} (°C)	T_{max} (°C)
Inside the drying chamber	T_{I1}	25.98	34.21	38.92
	T_{I2}	24.66	40.96	51.05
	T_{I3}	37.61	63.29	74.33
	T_{I4}	26.42	43.62	54.52
	T_{I5}	31.25	46.74	54.96
	T_{I6}	25.24	32.85	37.48
	T_{I7}	23.44	41.86	52.24
	T_{I8}	29.15	61.51	72.28
	T_{I9}	26.73	41.14	50.85
	T_{I10}	28.08	44.39	52.68
On the metal plates	T_{P1}	32.53	47.21	52.90
	T_{P2}	39.58	67.72	75.45
	T_{P3}	44.49	76.55	91.17
	T_{P4}	39.03	61.65	68.67
	T_{P5}	45.58	77.84	85.18
	T_{P6}	51.21	89.39	98.93
	T_{P7}	37.14	57.79	63.56
	T_{P8}	45.72	76.85	83.86

5.1.2. Second Configuration

Three tests were conducted in March 2023 using the second configuration for thermocouple location and by equipping the solar dryer with front and rear mirrors. Figure 11 shows the arrangement of thermocouples in this series of tests. This configuration comprised the same thermocouples used in the first configuration but placed at different points of the device, as evident in Figure 11.

A test was carried out on 13 March 2023 from 09:33 to 13:28 local time. During the test, the average normal direct solar radiation was about 750 W/m^2, while the average ambient temperature was about 18.5 °C. A second test performed on 22 March 2023 started at 09:55 and ended at 14:12 local time. During the second test, the average normal direct solar radiation was about 725 W/m^2, while the average ambient temperature was about 18.0 °C. The third test was performed on 23 March 2023 from 10:55 to 15:40 local time. During this last test, the average normal direct solar radiation was about 700 W/m^2, while the average ambient temperature was about 24.0 °C.

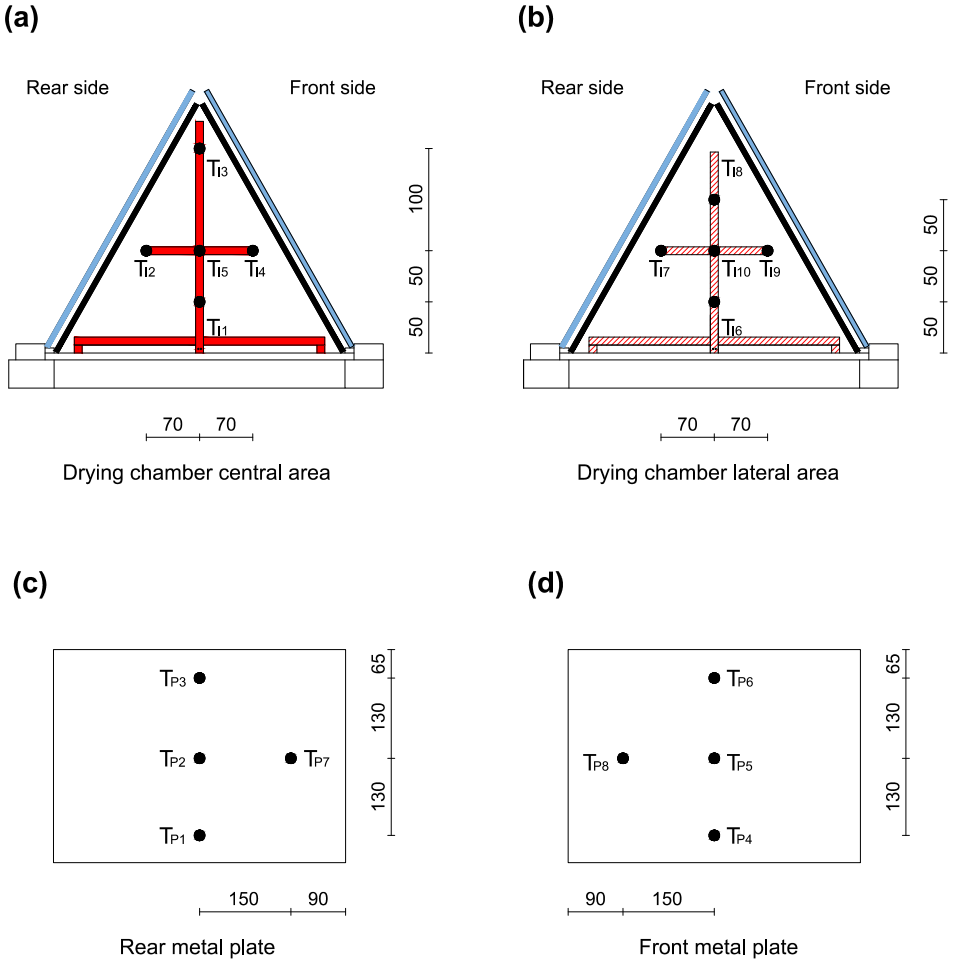

Figure 11. Position of the thermocouples for the March 2023 tests: (**a**) in the central area of the drying chamber; (**b**) in the lateral area of the drying chamber; (**c**) on the rear metal plate; (**d**) on the front metal plate. The dimensions are in mm. The thermocouple supports and the glass plates are highlighted in red and blue, respectively.

Table 2 shows the minimum, average, and maximum values of each temperature recorded during the three tests. The results show that the device used with the front and rear mirrors is able, in all three tests, to maintain internal temperatures suitable for drying (above 35–40 °C and below 70 °C) except in the upper part of the drying chamber, where temperatures well above 70 °C are reached. This outcome proves that the food should be appropriately placed inside the chamber to avoid spoiling it.

As an example, Figure 12 shows the trends of temperatures recorded inside the drying chamber (Figure 12a) and on the metal plates (Figure 12b), together with the trends of ambient temperature (T_{amb}) and direct normal solar irradiance (G_{bn}) for the test on 22 March 2023. The behaviors shown in this figure confirm that the temperature values in the drying chamber were generally suitable for drying foods, except in the upper part.

Table 2. Temperatures recorded on the thermal tests of March 2023 using the second configuration of the thermocouples.

		13 March 2023 $T_{amb,av}$ **= 18.51 °C and** $G_{bn,av}$ **= 749.93 W/m²**			**22 March 2023** $T_{amb,av}$ **= 18.40 °C and** $G_{bn,av}$ **= 725.25 W/m²**			**23 March 2023** $T_{amb,av}$ **= 23.82 °C and** $G_{bn,av}$ **= 702.10 W/m²**		
Recorded Temperatures	**Items**	T_{min} **(°C)**	T_{av} **(°C)**	T_{max} **(°C)**	T_{min} **(°C)**	T_{av} **(°C)**	T_{max} **(°C)**	T_{min} **(°C)**	T_{av} **(°C)**	T_{max} **(°C)**
Inside the drying chamber	T_{I1}	27.40	42.80	49.07	35.76	45.06	51.43	39.25	48.69	55.66
	T_{I2}	27.16	50.83	64.85	39.80	57.86	68.43	48.20	58.73	78.28
	T_{I3}	42.36	72.72	83.52	64.48	80.57	90.72	65.23	84.02	94.43
	T_{I4}	35.15	53.65	63.75	42.57	58.73	67.82	44.95	60.20	76.64
	T_{I5}	31.18	56.32	65.26	48.31	62.39	69.89	49.38	65.39	75.52
	T_{I6}	26.27	40.10	46.23	34.60	42.63	47.72	37.72	46.29	54.00
	T_{I7}	28.34	51.92	64.66	41.82	58.19	67.17	50.36	60.07	79.05
	T_{I8}	43.13	70.85	82.75	60.50	78.09	88.06	66.57	81.19	94.35
	T_{I9}	35.14	52.81	63.41	44.51	57.50	66.47	48.43	59.87	76.52
	T_{I10}	30.49	53.74	62.44	47.78	59.31	66.77	48.45	62.47	73.31
On the metal plates	T_{P1}	37.14	54.74	60.79	50.86	55.51	61.93	49.81	58.06	66.43
	T_{P2}	51.55	75.26	83.82	74.72	83.72	93.21	76.31	89.00	95.69
	T_{P3}	58.55	82.52	95.37	78.46	96.83	110.81	84.31	101.90	109.23
	T_{P4}	55.29	74.95	83.31	63.27	78.71	87.16	67.66	83.20	89.05
	T_{P5}	69.67	90.58	97.72	73.48	93.84	102.33	77.47	97.78	103.98
	T_{P6}	75.21	100.16	107.31	84.73	106.53	117.37	86.84	111.29	118.60
	T_{P7}	43.36	70.46	77.85	64.61	74.06	80.79	67.45	78.30	88.23
	T_{P8}	66.54	90.10	97.76	78.92	93.36	101.26	79.51	99.20	105.34

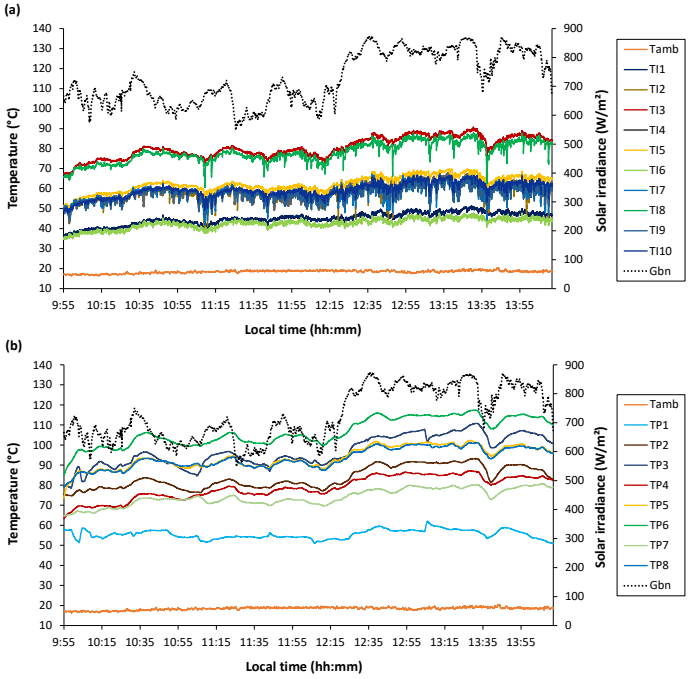

Figure 12. Temperature trends recorded during the thermal test of 22 March 2023: (**a**) internal temperatures inside the drying chamber; (**b**) plate temperatures. The ambient temperature and direct solar irradiance trends are also reported. The positions of the recorded temperatures are shown in Figure 11.

5.1.3. Third Configuration

One test with the third configuration for the location of the thermocouples was conducted on 18 July 2023 using the solar dryer without front and rear mirrors. Figure 13 shows the position of thermocouples in this test:

(a) At the base of the drying chamber, four thermocouples were attached to record the temperature of the air entering the chamber (T_{A1}, T_{A2}, T_{A3}, and T_{A4}).

(b) Four thermocouples were attached to a wooden support placed in the central area of the drying chamber to record the internal temperatures (T_{I1}, T_{I2}, T_{I3}, and T_{I4}). Six thermocouples were placed on the metal plates (T_{P1}, T_{P2}, T_{P3}, T_{P4}, T_{P5}, and T_{P6}). Two thermocouples were placed on the glass plates (T_{G1} and T_{G2}). One was placed in the upper region between the plates and the glass panes to measure the air leaving the drying chamber (T_{A5}).

(c) In the lateral area of the drying chamber, four thermocouples were attached to a wooden support inside the chamber to record the internal temperatures (T_{I5}, T_{I6}, T_{I7}, and T_{I8}) and one, placed in the upper region between the plates and the glass panes, to measure the air leaving the drying chamber (T_{A6}).

The test started at noon and ended at 14:06, local time. The average normal direct solar irradiance was about 752 W/m^2, while the average ambient temperature was about 32.5 °C.

Table 3 shows the minimum, average, and maximum values of each temperature recorded during the entire test. Figure 14 shows the temperature trends recorded inside the chamber (Figure 14a), on the plates (Figure 14b), on the glass panes (Figure 14c), and of the air entering and leaving the drying chamber (Figure 14d), along with the trends of ambient temperature (T_{amb}) and direct normal solar irradiance (G_{bn}).

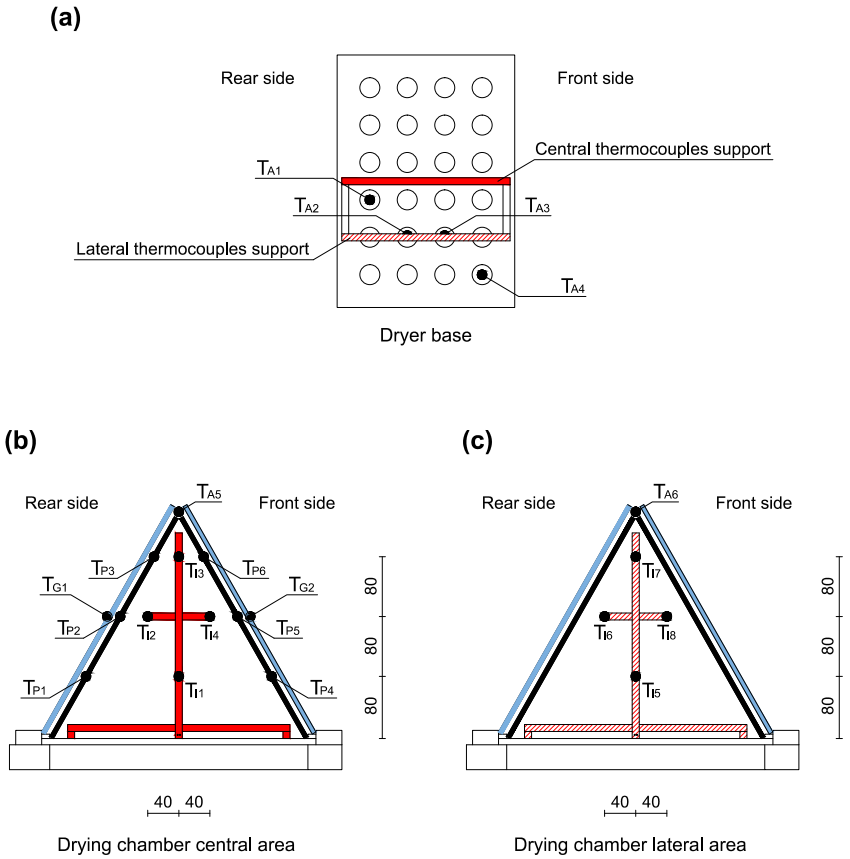

Figure 13. Position of the thermocouples for the 18 July 2023 test: (**a**) at the dryer base; (**b**) in the central area of the drying chamber; (**c**) in the lateral area of the drying chamber. The dimensions are in mm. The thermocouple supports and the glass plates are highlighted in red and blue, respectively.

Table 3. Temperatures recorded on the thermal test of 18 July 2023 using the third configuration of the thermocouples.

		18 July 2023 $T_{amb,av}$ **= 32.53 °C and** $G_{bn,av}$ **= 751.62 W/m²**		
Recorded Temperatures	**Items**	T_{min} **(°C)**	T_{av} **(°C)**	T_{max} **(°C)**
Inside the drying chamber	T_{I1}	41.16	44.14	46.31
	T_{I2}	45.01	48.81	54.26
	T_{I3}	49.34	53.61	59.66
	T_{I4}	43.98	48.23	53.00
	T_{I5}	43.85	47.05	49.42
	T_{I6}	44.94	48.77	52.95
	T_{I7}	48.58	54.70	59.98
	T_{I8}	44.62	48.77	52.21
On the metal plates	T_{P1}	46.54	49.60	52.39
	T_{P2}	49.20	51.88	54.73
	T_{P3}	52.41	55.14	58.52
	T_{P4}	66.69	69.76	73.27
	T_{P5}	69.00	71.87	75.00
	T_{P6}	71.91	75.36	78.50
On the glass plates	T_{G1}	40.81	44.14	47.20
	T_{G2}	51.10	54.47	57.70
Of inlet air	T_{A1}	35.32	38.81	41.88
	T_{A2}	36.12	39.47	41.76
	T_{A3}	38.03	40.84	43.54
	T_{A4}	35.93	39.31	42.83
Of outlet air	T_{A5}	38.85	49.60	58.98
	T_{A6}	44.30	50.69	57.63

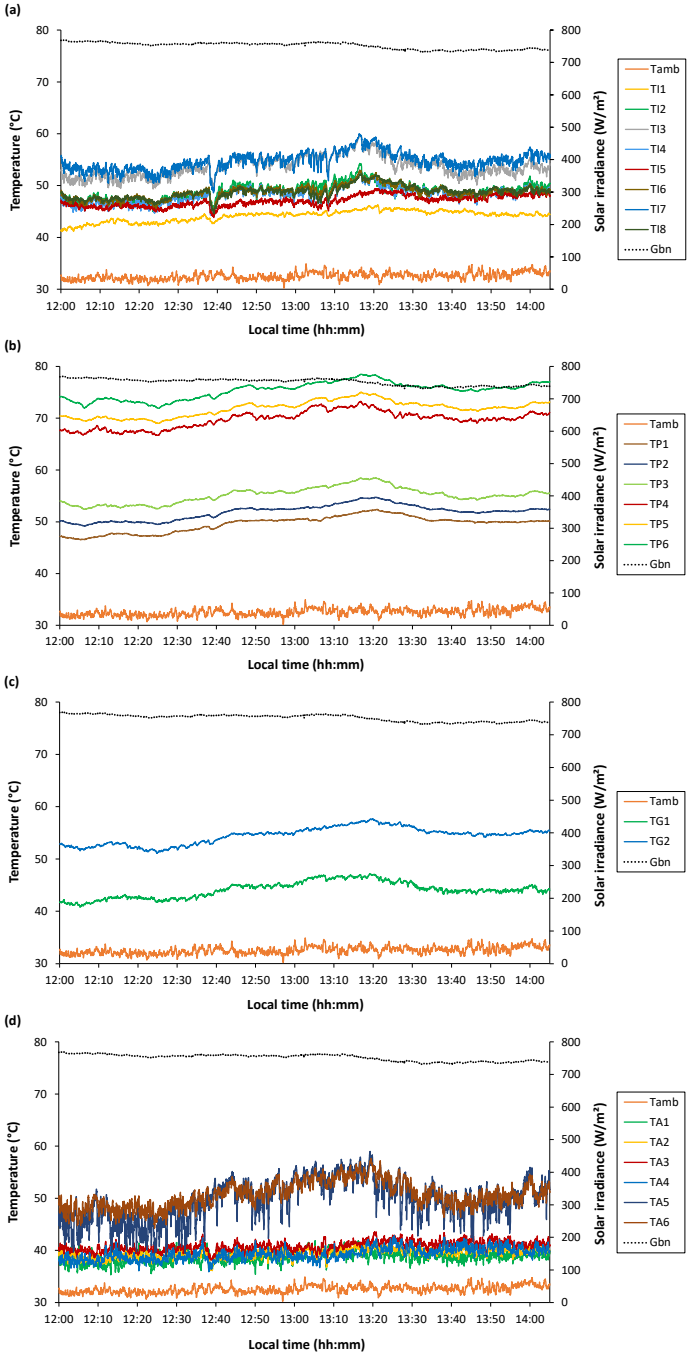

Figure 14. Temperature trends recorded during the thermal test of 18 July 2023: (**a**) temperatures inside the drying chamber; (**b**) temperatures on the plates; (**c**) temperatures on the glass panes; (**d**) temperatures of the air entering and leaving the drying chamber. The ambient temperature and direct solar irradiance trends are also reported. The positions of the recorded temperatures are shown in Figure 13.

From Table 3 and Figure 14, it is possible to note that the temperature inside the drying chamber was maintained between a range of about 41 °C to 60 °C during all the tests. In detail, there is an even distribution between the central and lateral areas with a difference between the top and bottom of the drying chamber of about 10 °C and substantial uniformity in the horizontal plane (T_{I2av}, T_{I4av}, T_{I6av}, and T_{I8av} of Table 3). It is also evident that there is a vertical temperature gradient. Regarding the average temperature trends on the metal plates, there is the presence of a vertical gradient on each plate and a temperature difference between the front plate (T_{P4}, T_{P5}, and T_{P6}) and the rear plate

(T_{P1}, T_{P2}, and T_{P3}) of about 20 °C. There is also a difference of about 10 °C between the average temperatures recorded in the middle zones of the front and rear glass plates. The average inlet air temperatures are found to be uniform. Similarly, the average outlet air temperatures between the central and lateral parts of the drying chamber were uniform. These temperature values prove the device is suitable for food drying in this configuration.

5.2. Drying Tests

This section reports the outdoor drying tests carried out using the dryer equipped with the front and rear mirrors and loaded with the following foods: apples, peas, spinach, and tomatoes. Each food was dried on different consecutive days needed to ensure its complete drying. At the end of each drying day, the product was stored inside airtight containers. This procedure prevented the partially dried product from absorbing moisture from the surrounding environment. The masses of the product were measured at the beginning and end of each drying test. In particular, frozen peas, spinach, and tomatoes were used in the tests to comply with the industrial drying processes.

5.2.1. Apples

Three tests to dry apples were carried out on three consecutive days in October 2022. The drying chamber was loaded during the first test with an initial mass of 255 g of apples cut into slices about 5 mm thick. The slices were placed on two trays loaded into the drying chamber, as shown in Figure 15.

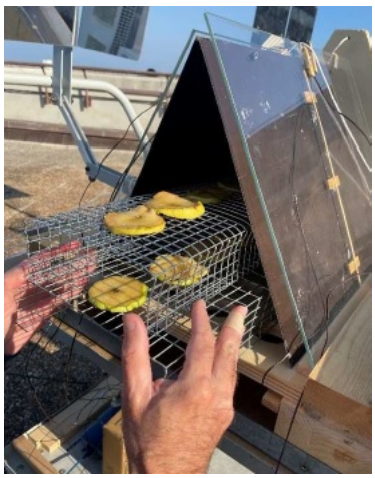

Figure 15. Trays with apple slices loaded inside the drying chamber.

Figure 16 shows the arrangement of thermocouples in the tests. In the central area of the drying chamber, one thermocouple was placed under the upper tray (T_{I1}) and one under the lower tray (T_{I2}). In addition, one thermocouple was placed in the upper region between the plates and the glass panes to measure the air leaving the drying chamber (T_{A1}). Two thermocouples were placed in the center of each metal plate: T_{P1} in the rear plate and T_{P2} in the front plate, respectively.

The first test was conducted on 17 October 2022 from 12:05 to 16:05 local time. During the test, the average normal direct solar radiation was about 776 W/m^2, while the average ambient temperature was about 20 °C. The second test was conducted on 18 October 2022, starting at 10:15 and ending at 14:15 local time. The average normal direct solar radiation and the average ambient temperature of the second test were about 739 W/m^2 and 20 °C, respectively. The last test was carried out on 19 October 2022 from 10:27 to 14:35 local time. During the test, the average normal direct solar radiation was about 612 W/m^2, while the average ambient temperature was about 20 °C.

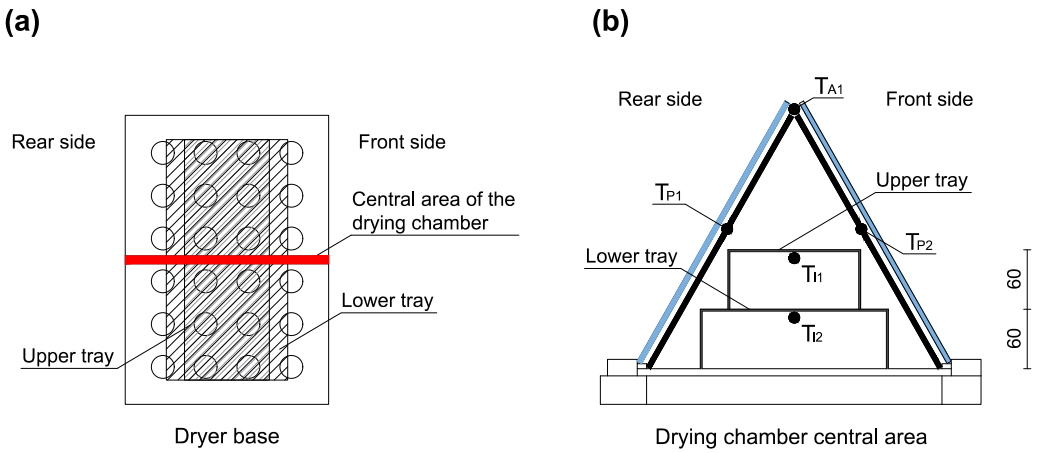

Figure 16. Position of thermocouples during apple drying tests: (**a**) dryer base and (**b**) drying chamber central area. The dimensions are in mm. The glass plates are highlighted in blue.

Table 4 shows the minimum, average, and maximum values of each temperature recorded during the tests. On the other hand, Table 5 shows the masses of apple slices used during the tests along with their percentage reduction. In three days of drying, there was a total reduction of 82 % in the mass of apples placed on the trays. This result proves the ability of the proposed device to dry apples under the outdoor conditions of the tests.

Table 4. Temperatures recorded during the apple drying tests.

		17 October 2022 $T_{amb,av}$ **= 20.24 °C and** $G_{bn,av}$ **= 775.89 W/m²**			**18 October 2022** $T_{amb,av}$ **= 19.74 °C and** $G_{bn,av}$ **= 738.61 W/m²**			**19 October 2022** $T_{amb,av}$ **= 19.69 °C and** $G_{bn,av}$ **= 611.88 W/m²**		
Recorded Temperatures	**Items**	T_{min} **(°C)**	T_{av} **(°C)**	T_{max} **(°C)**	T_{min} **(°C)**	T_{av} **(°C)**	T_{max} **(°C)**	T_{min} **(°C)**	T_{av} **(°C)**	T_{max} **(°C)**
Inside the drying chamber	T_{I1}	49.37	71.32	82.86	50.69	65.04	74.84	31.50	50.77	65.06
	T_{I2}	39.44	48.32	52.79	39.06	51.29	58.81	29.98	43.02	51.87
On the metal plates	T_{P1}	62.02	83.18	89.64	60.61	81.79	90.24	54.75	70.78	83.14
	T_{P2}	73.25	96.04	103.87	77.45	92.15	95.97	67.15	84.38	93.59
Of outlet air	T_{A1}	49.96	73.19	82.09	58.50	73.19	79.03	39.29	59.15	69.92

Table 5. Total mass of apples and its percentage reduction in the three tests performed.

Date	**Start Time**	**End Time**	**Initial Mass (g)**	**Final Mass (g)**	**Mass Reduction (%)**
17 October 2022	12:05	16:05	255.0	144.3	43
18 October 2022	10:15	14:15	144.3	75.4	48
19 October 2022	10:27	14:35	75.4	45.1	40

5.2.2. Peas

Three tests for drying peas were carried out on three consecutive days in June 2023. The drying chamber was loaded during the first test with an initial mass of 888 g of peas. Figure 17 shows the arrangement of thermocouples in these three tests. At the base of the drying chamber, one thermocouple was attached to record the temperature of the air entering the chamber (T_{A1}). In the central area of the drying chamber, one thermocouple was placed under the upper tray (T_{I1}) and one under the lower tray (T_{I2}). One thermocouple was placed in the upper region between the plates and the glass panes to measure the air leaving the drying chamber (T_{A2}).

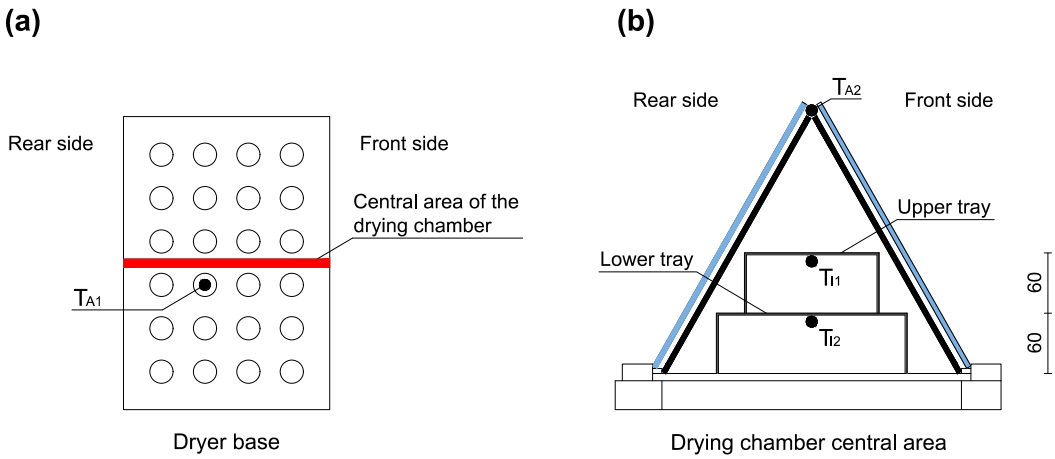

Figure 17. Position of thermocouples during pea drying tests: (**a**) dryer base and (**b**) drying chamber central area. The dimensions are in mm. The glass plates are highlighted in blue.

The first test was performed on 7 June 2023 from 11:10 to 16:40 local time. During the test, the average normal direct solar radiation and the average ambient temperature were about 802 W/m^2 and 26.6 °C, respectively. The second test was carried out on 8 June 2023, starting at 10:03 and ending at 15:33 local time. The average normal direct solar radiation of this test was about 828 W/m^2, while the average ambient temperature was about 25.8 °C. The third test was conducted on 9 June 2023 from 09:52 to 15:38 local time. The average normal direct solar radiation of the third test was about 790 W/m^2, while the average ambient temperature was about 28 °C.

Table 6 shows the minimum, average, and maximum values of each temperature recorded during the tests. Table 7, on the other hand, shows the masses of the peas used during the tests along with their percentage reduction. In three days of drying, there was a total reduction in the mass of peas placed in the upper tray of 78% and one of 74% in the lower tray. Considering that a longer drying time was needed since a frozen product was tested, these outcomes demonstrate that the proposed solar dryer is able to dry peas.

Table 6. Temperatures recorded during the pea drying tests.

		7 June 2023 $T_{amb,av}$ **= 26.58 °C and** $G_{bn,av}$ **= 802.38 W/m^2**			**8 June 2023** $T_{amb,av}$ **= 25.75 °C and** $G_{bn,av}$ **= 828.43 W/m^2**			**9 June 2023** $T_{amb,av}$ **= 27.98 °C and** $G_{bn,av}$ **= 789.78 W/m^2**		
Recorded Temperatures	**Items**	T_{min} **(°C)**	T_{av} **(°C)**	T_{max} **(°C)**	T_{min} **(°C)**	T_{av} **(°C)**	T_{max} **(°C)**	T_{min} **(°C)**	T_{av} **(°C)**	T_{max} **(°C)**
Inside the drying chamber	T_{I1}	40.10	60.41	72.74	33.59	58.33	69.57	50.07	62.57	72.72
	T_{I2}	21.37	41.70	47.71	27.87	45.94	50.98	39.48	49.01	55.13
Of inlet air	T_{A1}	23.12	27.57	31.01	24.79	28.32	30.97	25.98	30.90	35.76
Of outlet air	T_{A2}	50.66	80.62	96.00	52.33	78.61	90.98	59.40	78.72	94.94

Table 7. Pea mass reduction over three days for the upper and lower trays.

Date	**Start Time**	**End Time**	**Initial Mass (g)**	**Final Mass (g)**	**Mass Reduction (%)**
			Upper tray		
7 June 2023	11:10	16:40	436	292	33
8 June 2023	10:03	15:33	292	116	60
9 June 2023	09:52	15:38	116	96	17
			Lower tray		
7 June 2023	11:10	16:40	452	364	19
8 June 2023	10:03	15:33	364	224	38
9 June 2023	09:52	15:38	224	116	48

5.2.3. Spinach

Two tests to dry spinach were carried out on two consecutive days in June 2023. The drying chamber was loaded during the first test with an initial mass of 104 g of spinach placed on the top tray. During the tests, the thermocouples were arranged as for the pea tests (Figure 17), excluding the thermocouple T_{I2}.

The first test was conducted on 20 June 2023 from 10:33 to 15:39 local time. During this test, the average normal direct solar radiation and the average ambient temperature were about 608 W/m^2 and 32.6 °C, respectively. The second test was conducted on 21 June 2023, starting at 10:47 and ending at 13:24 local time. The average normal direct solar radiation of the second test was about 608 W/m^2, while the average ambient temperature was about 31.9 °C.

Table 8 shows the minimum, average, and maximum values of each temperature recorded during the tests. Table 9, on the other hand, shows the masses of spinach used during the tests along with their percentage reduction. In two days of drying, there was a total reduction in spinach mass of 91 %, proving that the product was well dried.

Table 8. Temperatures recorded during the spinach drying tests.

		20 June 2023 $T_{amb,av}$ **= 32.64 °C and** $G_{bn,av}$ **= 607.52 W/m^2**			**21 June 2023** $T_{amb,av}$ **= 31.86 °C and** $G_{bn,av}$ **= 608.43 W/m^2**		
Recorded Temperatures	**Items**	T_{min} **(°C)**	T_{av} **(°C)**	T_{max} **(°C)**	T_{min} **(°C)**	T_{av} **(°C)**	T_{max} **(°C)**
Inside the drying chamber	T_{I1}	26.69	59.66	81.54	36.63	61.72	78.74
Of inlet air	T_{A1}	26.46	36.45	40.28	34.35	37.47	40.05
Of outlet air	T_{A2}	26.49	74.55	86.43	36.00	73.63	91.33

Table 9. Spinach mass reduction over two days for the upper tray.

Date	**Start Time**	**End Time**	**Initial Mass (g)**	**Final Mass (g)**	**Mass Reduction (%)**
20 June 2023	10:33	15:39	104	11.5	89
21 June 2023	10:47	13:24	11.5	9	22

5.2.4. Tomatoes

Three tests to dry tomatoes were carried out on three consecutive days in June 2023. The drying chamber was loaded during the first test with an initial mass of 148 g of cherry tomatoes sliced in half and placed on the top tray. During the tests, the thermocouples were placed exactly as for the pea and spinach tests (Figure 17).

The first test was performed on 26 June 2023 from 10:35 to 15:35 local time, and the average normal direct solar radiation and the average ambient temperature were about 859 W/m^2 and 28 °C, respectively. The second test was conducted on 27 June 2023 from 10:32 to 15:09 local time. During the second test, the average normal direct solar radiation was about 723 W/m^2, while the average ambient temperature was about 35 °C. The third test was carried out on 28 June 2023 from 10:18 to 12:37, local time. The average normal direct solar radiation of this last test was about 550 W/m^2, while the average ambient temperature was about 29 °C.

Table 10 shows the minimum, average, and maximum values of each temperature recorded during the tests. Table 11, on the other hand, shows the masses of tomatoes used during the tests along with their percentage reduction. The ability of the device to also dry tomatoes, despite them being frozen, was proved by the total reduction in tomato mass of 89% obtained in three days of drying.

Table 10. Temperatures recorded during the tomatoes drying tests.

		26 June 2023 $T_{amb,av}$ = 28.20 °C and $G_{bn,av}$ = 858.70 W/m^2			27 June 2023 $T_{amb,av}$ = 34.84 °C and $G_{bn,av}$ = 723.25 W/m^2			28 June 2023 $T_{amb,av}$ = 29.14 °C and $G_{bn,av}$ = 551.20 W/m^2		
Recorded Temperatures	**Items**	T_{min} (°C)	T_{av} (°C)	T_{max} (°C)	T_{min} (°C)	T_{av} (°C)	T_{max} (°C)	T_{min} (°C)	T_{av} (°C)	T_{max} (°C)
Inside the drying chamber	T_{I1}	23.06	58.79	77.17	57.87	64.38	69.46	29.72	51.78	69.21
Of inlet air	T_{A1}	24.66	36.36	43.39	33.63	38.90	42.24	26.26	30.73	34.17
Of outlet air	T_{A2}	31.76	69.49	95.25	70.71	77.73	89.26	29.78	63.70	91.54

Table 11. Tomatoe mass reduction over three days for the upper tray.

Date	Start Time	End Time	Initial Mass (g)	Final Mass (g)	Mass Reduction (%)
26 June 2023	10:35	15:35	148	52	65
27 June 2023	10:32	15:09	52	18	65
28 June 2023	10:18	12:37	18	16	11

6. Numerical Analysis

This section is aimed at describing the numerical setup used to analyze the solar dryer by means of Computational Fluid Dynamics (CFD), together with the results provided by the model. This preliminary study will provide the direction for future improvement in effective dryer design, with the final goal to optimize solar energy utilization.

6.1. Cfd Modelling

The numerical analysis of the solar dryer is focused on predicting its performance in its simplest configuration, corresponding to the dryer system without the mirrors. In fact, as it has been shown in Section 5.1.3 thanks to the experimental investigation, even without the use of the mirrors, with high/moderate solar radiation, the temperatures achieved inside the dryer are in the range of the usual temperature necessary to dry fruit/vegetable, i.e., 40–70 °C.

The simulations are performed with the commercial ANSYS Fluent 2023 R1 software based on the Finite Volume Method (FVM). Figure 18a shows the computational domain and the boundaries of the CFD modeling; Figure 18b shows the mesh used to perform the numerical analysis. The computational domain is the 3D model of the dryer with real dimensions (1:1 scale) that, given both the symmetry of the inlet conditions and of the dryer geometry with respect to the *xz* plane, has been halved to reduce the computational time necessary to perform the simulations. Furthermore, in Figure 18a, inlet (blue), outlet (red), and symmetry (orange) boundaries are highlighted. All the other boundaries, corresponding to solid surfaces, have been set to no-slip walls. In particular, while the wood structure has been modeled as a solid volume, the aluminum and glass surfaces have been modeled as shell conduction zones of thickness 0.001 and 0.004 m, respectively, using four layers for both. For both inlet and outlet boundary conditions, ambient pressure (101,325 Pa) and measured ambient temperature (32.2 °C) have been imposed. Note that for the outlet boundary, the temperature is needed only in case of backflow condition, which is not the case for the present study. The computational domain has been discretized with three different grids in order to perform a mesh independence study for optimizing the number of elements of the mesh and hence the computational time needed by the simulations. To perform this study, we have analyzed the temperature values obtained by using three meshes, named M1 (∼775,500 elements), M2 (∼896,000 elements), and M3 (∼1,308,000 elements). In particular, we have examined the numerical values of temperature at the experimental points, which are shown and labelled in the schematic layout of Figure 13. Table 12 shows the percentage variation of the temperature obtained by the simulations (note that all the percentage variations reported in this work are computed considering the temperature in °C). By looking at the table, we can conclude that the sensitivity of the solution to a better grid refinement is quite high and not negligible for M1 discretization, whereas the comparison between the temperatures obtained with M2

and M3 meshes shows a sensible better agreement. In fact, to have a general overview of the entries of the two tables, note that for meshes M1 and M2, the maximum and average variations are equal to 20.9% and $\sim$ 8.1%, respectively, while the same values are equal to only 6.9% and $\sim$ 3.1% for meshes M2 and M3. Therefore, the discretization M2 has been chosen to perform the numerical analysis of the dryer, even considering that the simulation time required for the convergence of the results using the M3 mesh was significantly larger than the one required for the less refined computational grid. M2 spatial discretization, see Figure 18b, is conformal and hybrid, with a minimum, maximum, and average aspect ratio equal to 1.05, 740, and 104, respectively, and a minimum, maximum, and average skewness equal to 5×10^{-5}, 0.97, and 0.29, respectively.

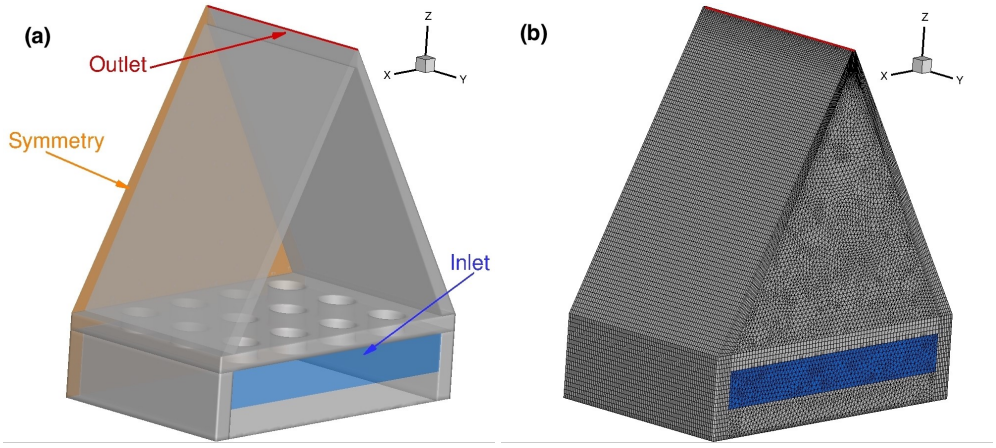

Figure 18. View of spatial discretization: (**a**) computational domain and boundaries and (**b**) mesh used to perform the numerical analysis.

Table 12. Mesh independence study.

M1 (775,500 elements) vs. M2 (896,000 elements)														
Point	T_{I1}	T_{I4}	T_{I2}	T_{I3}	T_{P4}	T_{P5}	T_{P6}	T_{P1}	T_{P2}	T_{P3}	T_{I5}	T_{I8}	T_{I7}	T_{I6}
Var.[%]	2.0	20.9	10.7	2.5	2.8	2.8	6.2	2.2	5.7	12.9	4.5	25	1.4	14.0
M2 (896,000) elements vs. M3 (1,308,000) elements														
Point	T_{I1}	T_{I4}	T_{I2}	T_{I3}	T_{P4}	T_{P5}	T_{P6}	T_{P1}	T_{P2}	T_{P3}	T_{I5}	T_{I8}	T_{I7}	T_{I6}
Var.[%]	6.9	3.1	1.9	5.5	0.4	0.6	0.7	0.6	3.9	4.9	5.4	3.6	1.3	4.9

The simulations are performed under steady, viscous, incompressible, and laminar flow assumptions, and, to model the natural convection, the Boussinesq approximation is used. In particular, the laminar flow assumption is justified by the value of the Rayleigh number computed as follows:

$$Ra = \frac{g\beta\Delta T L^3}{\nu\alpha}, \quad (1)$$

where g is the gravitational acceleration, β is the thermal expansion coefficient, L is the height of the drying chamber, α is the thermal diffusivity, ν is the kinematic viscosity, and $\Delta T = T_h - T_c$, where T_h and T_c are the temperatures of the hot and cold absorbent surfaces, respectively. For both these temperatures, the experimentally measured values have been considered, i.e., for T_h the value considered is the average of the temperature measured at points T_{P4}, T_{P5}, and T_{P6}, equal to 72 °C, and for T_c, the value considered is the average of the temperature measured at points T_{P1}, T_{P2}, and T_{P3}, equal to 52 °C. The properties of air are evaluated at the mean temperature $T_0 = (T_h + T_c)/2 = 62$ °C and are reported in Table 13, together with the properties of the materials used for the absorbent surfaces (aluminum), the external surfaces used to create the greenhouse effect (glass), and all the other solid surfaces (wood). Note that for aluminum and wood, these values are taken from Fluent database materials, whereas for the glass, since this material is not present in the same database, these values have been imposed on the basis of literature data; e.g., the

thermal conductivity is between 0.9 and 1.2 W/mK for the most commonly used silicate glasses; therefore, the value of 1.0 W/mK has been chosen. The Rayleigh number (Ra) of the case here presented, computed using the air properties reported in the table, is about 3×10^7, which is well below the value that identifies the turbulent nature of the flow, i.e., $Ra > 10^9$.

Table 13. Fluid and solids properties.

Material	Property	Value
Air modelled as steady viscous, laminar and incompressible with Boussinesq flow assumption	Density ρ_0	1.053 kg/m^3
	Kinematic viscosity ν	2.0237×10^{-5} m^2/s
	Thermal conductivity k	2.8534×10^{-2} W/mK
	Thermal expansion coeff. β	2.9837×10^{-3} 1/K
	Specific heats c_p	1008.4 J/kgK
Aluminium surfaces modelled as shell conduction zones of thickness 0.001 m	Density ρ	2719 kg/m^3
	Specific heats c_p	871 J/kgK
	Thermal conductivity k	202.4 W/mK
Glass surfaces modelled as shell conduction zones of thickness 0.004 m	Density ρ	2321 kg/m^3
	Specific heats c_p	840 J/kgK
	Thermal conductivity k	1 W/mK
Wood modelled as a solid volume	Density ρ	700 kg/m^3
	Specific heats c_p	2310 J/kgK
	Thermal conductivity k	0.173 W/mK

The Boussinesq approximation is often used in CFD since it allows one not to consider the full compressible Navier–Stokes equations, getting faster convergence with a good approximation of density and, therefore, quite accurate numerical results. This approximation assumes that the density variation has only one effect on the flow field, i.e., it gives rise to buoyancy forces. Its accuracy is strongly related to the validity of the linear assumption between temperature and density that it introduces, that is reported here:

$$\rho = \rho_0 - \beta\rho_0(T - T_0). \tag{2}$$

Therefore, the Boussinesq approximation is much more valid when temperature and therefore density variations are small, which is exactly the case of this study, since

$$\Delta T\beta \sim 0.06. \tag{3}$$

The equations governing the behavior of viscous, incompressible, and laminar flows are the Navier–Stokes equations (continuity, momentum, and energy equations), which, taking into account the Boussinesq approximation, can be written as follows:

$$\begin{aligned} &\nabla \cdot \mathbf{u} = 0, \\ &\frac{\partial \mathbf{u}}{\partial t} + \mathbf{u} \cdot \nabla \mathbf{u} = -\frac{1}{\rho_0}\nabla(p - \rho_0 \mathbf{g} \cdot \mathbf{z}) + \nu\nabla^2\mathbf{u} - \mathbf{g}\beta(T - T_0) = 0, \\ &\frac{\partial T}{\partial t} + \mathbf{u} \cdot \nabla T = \frac{k}{\rho c_p}\nabla^2 T + \frac{J}{\rho c_p}, \end{aligned} \tag{4}$$

where $\mathbf{u}$ is the velocity vector, p is the pressure, $\mathbf{z}$ is a vector with the only non-zero component equal to the vertical distance measured from any convenient horizontal, i.e., xy, reference plane, $\mathbf{g} = (0, 0, -g)$, $\rho = \rho_0 - \beta\rho_0(T - T_0)$, and J is the rate per unit volume of internal heat production. Please note that for the definition of $\mathbf{z}$ and $\mathbf{g}$, we refer to the coordinate system reported in Figure 18.

To mimic the solar radiation, the ANSYS Fluent solar load model is used. In particular, the solar calculator utility, included in the solar load model, is used to define the location of the sun in the sky on the basis of user inputs, i.e., day, time, and position. Day and time are set to July 18 at 12:51 (note that the time has been calculated as the average time at which the experimental measurements, used to validate the numerical model, have been

collected, i.e., 12:46–12:56). Latitude and longitude values are set equal to 43.589 and 13.516, respectively. Furthermore, to determine the relative position of the sun with respect to the computational domain, the mesh orientation has been given, and to match the measured value of the direct normal solar irradiation at the earth's surface, the sunshine factor has been used. This factor, which has to be set in the range [0–1], is a linear reduction factor of the computed solar irradiation to account, for example, for cloud cover. In the present study, the sunshine factor has to be set to 0.87 to match the measured direct normal solar irradiation at the earth's surface, equal to 757.5 W/m^2. Nevertheless, since the glasses were modeled as not participating in the solar radiation, the sunshine factor has been set equal to 0.78 to account for about 10% of the solar irradiation reflected by these external surfaces.

The Surface-to-Surface (S2S) model [31] has been used to take into account the radiation effects within the domain. This radiation model is a good compromise between accuracy and efficiency, and it is often used to compute the radiation exchange in an enclosure of gray-diffuse surfaces, like in this study. In fact, preliminary simulations conducted with the P1 radiation model [32] have predicted higher temperature values with respect to the experimental ones (note that this is consistent with what is reported in the literature and the results of many computations; see, for example, [33,34]). On the other hand, the Discrete Ordinates (DO) radiation model [35,36] has not been used in this work since, even if more accurate than the S2S model, it requires a much higher computational effort.

The discretization and solution schemes used for the simulations are as follows: for the pressure–velocity coupling, the Pressure-Implicit with Splitting of Operators (PISO) segregated solver [37]; for pressure, a body force weighted algorithm; and for momentum and energy equations, a third-order muscle scheme. Convergence was monitored by checking the scaled residual convergence history. Computations were continued until the residual curves reached plateau values and were reducing by five/six orders of magnitude (the plateau value for the continuity equation was about 3×10^{-5}, for the three momentum equations was in the range 2–5$\times 10^{-6}$, and for the energy equation was about 3×10^{-6}).

6.2. CFD Validation and Analysis of the Results

To validate the accuracy of the numerical analysis (mesh, material properties, numerical algorithms, and other input necessary to perform the simulations), in Table 14 it is shown the comparison between the predicted (Num.) and the measured (Exp.) temperatures. In particular, in the last row of the table, the absolute value of the percentage variation between the two data points (Var.) is reported for several points, which are labelled in the first row of the table (Point). Note that in this table the points used to validate the CFD analysis are labelled as already shown in Figure 13. By looking at the percentage variations reported in this table, it is possible to conclude that CFD results show generally good agreement with respect to the experimental data, with a global average error equal to about 3.6%. Furthermore, it is possible to note that the larger differences between the predicted and the experimental temperatures were measured in the upper part of the dryer, i.e., points T_{I3}, T_{P6}, T_{P3}, and T_{I7} (please see Figure 13), while in the rest of the dryer the agreement between the two data is significantly better. This behavior is justified by the higher flow field complexity that occurs in the upper part of the dryer, and that is highlighted in what follows.

Table 14. Validation of CFD analysis.

Numerical vs. Experimental Temperatures [°C].														
Point	T_{I1}	T_{I4}	T_{I2}	T_{I3}	T_{P4}	T_{P5}	T_{P6}	T_{P1}	T_{P2}	T_{P3}	T_{I5}	T_{I8}	T_{I6}	T_{I7}
Exp.	44.5	49.0	49.5	54.8	70.4	72.5	75.9	50.2	52.5	55.8	46.9	49.1	49.2	55.1
Num.	46.1	50.7	51.2	51.7	69.0	71.5	71.0	49.3	51.0	51.0	46.9	50.4	51.5	52.7
Var.	3.6%	3.5%	3.4%	5.7%	2.0%	1.4%	6.5%	1.8%	2.9%	8.6%	0%	2.6%	4.7%	4.4%

Figure 19 shows the temperature contours on the planes illustrated in Figure 13 (central and lateral planes). It is observed in both the planes that there is a not-uniform temperature distribution along the z-axis direction, which is in agreement with the temperature values measured experimentally. This non-uniform distribution is unfavorable because the food positioned at different z-values may not dry evenly. However, at a given z-value, the temperature distribution is quite uniform, resulting in a uniform drying process for the food located along this plane. Furthermore, the temperature distribution reported in the plots suggests that, considering that the usual temperature to dry fruit/vegetable is in the range of 40–70 °C, the designed dryer, even without the mirrors, can be efficiently used, at least in the months of the year that correspond to a direct normal solar irradiation at the earth's surface that is around the measured value, i.e., 750 W/m^2, a value that is typically reached in summer at the latitude and longitude at which the dryer has been tested. Finally, even if the solar irradiation will be lower in other months of the year, for example in spring, the dryer could be efficiently used to produce raw dried food. In fact, during the drying process of raw food, the temperature must be below 42 °C in order to maintain its nutritional and organoleptic properties unaltered. Obviously, more in-depth studies are needed to explore this possibility, taking into account, for example, the time required by this particular drying process. To this regard, it is important to point out that the rate of the drying process strongly depends upon the thickness of the product. Therefore, the thickness of the food can be decided on the basis of the maximum time required by the process itself.

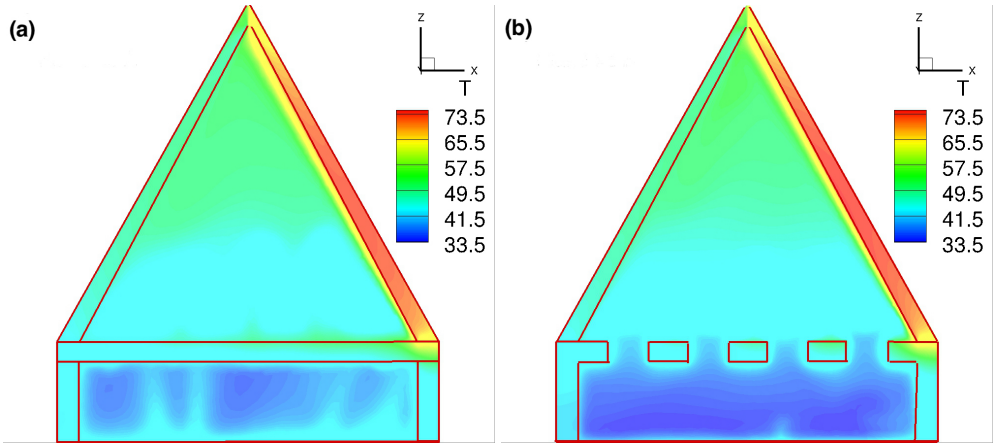

Figure 19. Temperature distribution (in °C) on (**a**) central plane and (**b**) lateral plane.

In Figures 20 and 21 are shown predicted velocity magnitude and velocity stream traces, respectively. From Figure 20 we can observe that air velocity in the dryer is quite small, with higher values that are reached by the fluid near the hot absorbent surface and the outflow. The stream traces, shown in Figure 21, put in evidence a large anticlockwise recirculating region in the upper part of the dryer, created by the movement of the flow that, before exiting, goes downward along the cold plate. The exact position of the recirculating zone, its size, and its strength depend on several factors, e.g., the temperature difference between the cold and the hot absorbent surfaces, the angle between them, and/or the height of the dryer, factors that could significantly improve the heat transfer.

Indeed, the final aim of this preliminary CFD study, here validated with experimental measurements, will be to identify potential improvements in dryer design, providing useful information on the main factors influencing its performance, and therefore, finally, to propose a clear improvement methodology for further research.

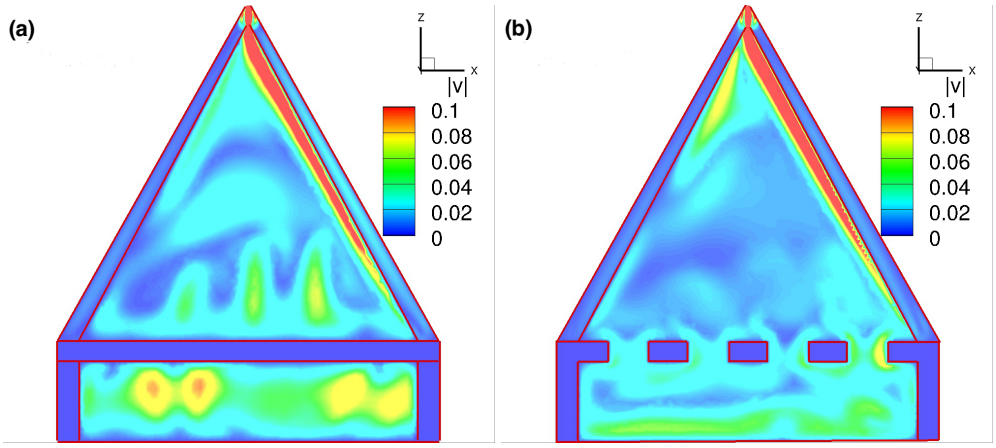

Figure 20. Velocity magnitude distribution (in m/s) on (**a**) central plane and (**b**) lateral plane.

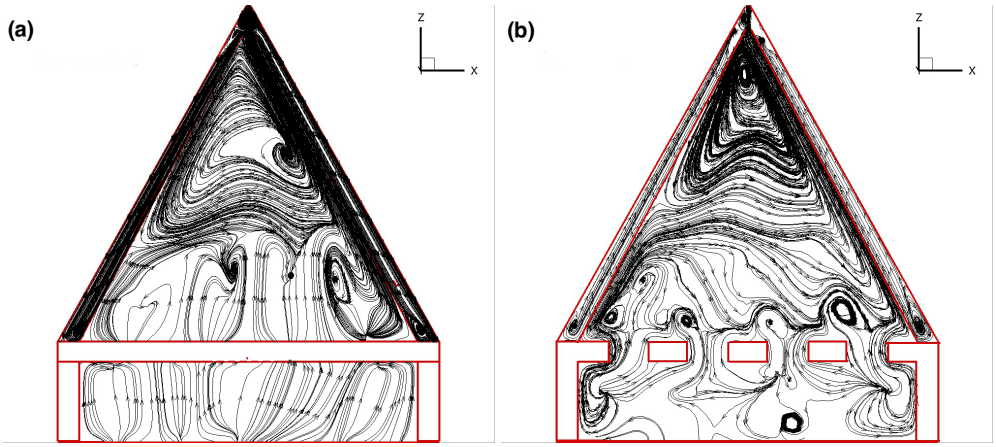

Figure 21. Stream traces on (**a**) central plane and (**b**) lateral plane.

7. Conclusions

In this work, a novel solar dryer has been presented and investigated experimentally and numerically. The device can be classified as an indirect passive solar dryer, where the product in the drying chamber is mainly heated by radiation from black metal plates that form the prism-shaped drying chamber, while the moisture is removed by a natural airflow. Its main features are ease of construction, since it has a simple design and is made of common and low-cost materials; a variable geometry to increase the concentration of solar radiation into the drying chamber; and ease of transport, assembly, and disassembly.

Two different types of experimental tests were carried out: thermal tests and drying tests. In the former, the device was tested without load to analyze its thermal behavior and the temperature gradients inside the drying chamber. Food drying tests were carried out by placing different masses of apples, peas, spinach, and tomatoes on one or two trays inside the drying chamber. In detail, each food was dried for some consecutive days, and the dried product was stored inside hermetically sealed containers after each drying cycle to avoid the absorption of moisture from the external environment.

The results of thermal tests showed that the device was able to maintain the temperatures inside the chamber in a range between 35 °C and 70 °C, suitable for drying food, even under less favorable environmental conditions. However, it is worth noting that, in some tests, the temperature in the upper part of the chamber was higher than 70 °C. This outcome proves that the design of the proposed solar dryer can be improved to obtain a more uniform temperature in the drying chamber.

The results of the drying tests showed the good drying efficiency of the device. It was found that, at the end of the drying period, each food had a total reduction in its mass

of between about 80–90% (82% for apples, 78% and 74% for frozen peas, 89% for cherry tomatoes, and 91% for frozen spinach).

A Computational Fluid Dynamics (CFD) analysis was conducted to predict the performance of the proposed solar dryer. The comparison between numerical and experimental temperatures showed good agreement. The simulations identified a low-speed recirculating zone in the upper part of the dryer, which promotes mixing between the airflow near the absorbent surface exposed to solar radiation and the opposite side, resulting in a more uniform temperature distribution.

Finally, it is important to note that this preliminary solar dryer has some limitations that may negatively affect its usability. Specifically, the prototype has a small drying chamber that, in some cases, reaches excessively high temperatures. This could lead to limited drying capacity and potential overheating of the product. To address these issues, future work will focus on optimizing the solar dryer's design to achieve a more uniform temperature distribution in the drying chamber, taking advantage of the information obtained from the CFD model. Additionally, a more comprehensive analysis of the natural airflow and moisture gradient within the drying chamber, as well as an assessment of the quality of the dried product, will be essential for better performance characterization.

Author Contributions: Conceptualization, P.F.M., S.T., and M.M.; methodology, P.F.M. and A.N.; software, A.N.; validation, P.F.M., A.N., A.A., and S.T.; formal analysis, P.F.M., A.N., and A.A.; investigation, P.F.M.; data curation, A.N.; writing—original draft preparation, P.F.M., A.N., and A.A.; writing—review and editing, A.N., S.T., and G.D.N.; visualization, A.N. and A.A.; supervision, G.D.N. and M.M. All authors have read and agreed to the published version of the manuscript.

Funding: This research received no external funding.

Data Availability Statement: The original contributions presented in this study are included in the article. Further inquiries can be directed to the corresponding author.

Conflicts of Interest: Author Matteo Muccioli was employed by the Studio MUMA. The remaining authors declare that the research was conducted in the absence of any commercial or financial relationships that could be construed as a potential conflict of interest.

Nomenclature

Latin Symbols	
c_p	Specific heat (J/(kg K))
g	Gravitational acceleration (m/s^2)
G_{bn}	Direct normal irradiance (W/m^2)
H_{sun}	Sun elevation (°)
J	Internal heat production rate per unit volume (W/m^3)
L	Drying chamber height (m)
M	Mesh
p	Pressure (Pa)
Ra	Rayleigh number
T	Temperature (°C)
$\boldsymbol{u}$	Velocity vector
Greek Symbols	
α	Thermal diffusivity (m^2/s)
β	Thermal expansion coefficient (1/K)
Δ	Difference
κ	Thermal conductivity (W/mK)
ν	Kinematic viscosity (m^2/s)
ρ	Density (°C/(kg/m^3))
Subscripts	
A	Air
Air_inlet	Inlet air
Air_outlet	Outlet air

amb	Ambient
av	Average
c	Cold
G	Glass
h	Hot
I	Internal
max	Maximum
min	Minimum
P	Plate

Acronyms	
CFD	Computational Fluid Dynamics
CPU	Central Processing Unit
DES	Detached Eddy Simulation
DO	Discrete Ordinates
FVM	Finite Volume Method
LES	Large Eddy Simulation
NIP	Normal incidence pyrheliometer
NSC	Newton solar cooker
NSD	Newton Solar Dryer
PISO	Pressure-Implicit with Splitting of Operators
PMMA	Polymethylmethacrylate
RANS	Reynolds Averaged Navier–Stokes
S2S	Surface-to-Surface

References

1. Ekechukwu, O.V.; Norton, B. Review of solar-energy drying systems ii: An overview of solar drying technology. *Energy Convers. Manag.* **1999**, *40*, 615–655. [CrossRef]
2. Kamarulzaman, A.; Hasanuzzaman, M.; Rahim, N. Global advancement of solar drying technologies and its future prospects: A review. *Sol. Energy* **2021**, *221*, 559–582. [CrossRef]
3. Kherrafi, M.A.; Benseddik, A.; Saim, R.; Bouregueba, A.; Badji, A.; Nettari, C.; Hasrane, I. Advancements in solar drying technologies: Design variations, hybrid systems, storage materials and numerical analysis: A review. *Sol. Energy* **2024**, *270*, 112383. [CrossRef]
4. Goel, V.; Dwivedi, A.; Mehra, K.S.; Pathak, S.K.; Tyagi, V.; Bhattacharyya, S.; Pandey, A. Solar drying systems for domestic/industrial purposes: A state-of-art review on topical progress and feasibility assessments. *Sol. Energy* **2024**, *267*, 112210. [CrossRef]
5. Mustayen, A.; Mekhilef, S.; Saidur, R. Performance study of different solar dryers: A review. *Renew. Sustain. Energy Rev.* **2014**, *34*, 463–470. [CrossRef]
6. Fernandes, L.; Tavares, P.B. A review on solar drying devices: Heat transfer, air movement and type of chambers. *Solar* **2024**, *4*, 15–24. [CrossRef]
7. El-Mesery, H.S.; El-Seesy, A.I.; Hu, Z.; Li, Y. Recent developments in solar drying technology of food and agricultural products: A review. *Renew. Sustain. Energy Rev.* **2022**, *157*, 112070. [CrossRef]
8. Jain, A.; Sharma, M.; Kumar, A.; Sharma, A.; Palamanit, A. Computational fluid dynamics simulation and energy analysis of domestic direct-type multi-shelf solar dryer. *J. Therm. Anal. Calorim.* **2019**, *136*, 173–184. [CrossRef]
9. Jain, R.; Paul, A.S.; Sharma, D.; Panwar, N.L. Enhancement in thermal performance of solar dryer through conduction mode for drying of agricultural produces. *Energy Nexus* **2023**, *9*, 100182. [CrossRef]
10. Téllez, M.C.; Figueroa, I.P.; Téllez, B.C.; Vidaña, E.C.L.; Ortiz, A.L. Solar drying of stevia (rebaudiana bertoni) leaves using direct and indirect technologies. *Sol. Energy* **2018**, *159*, 898–907. [CrossRef]
11. Haque, T.; Tiwari, M.; Bose, M.; Kedare, S.B. Drying kinetics, quality and economic analysis of a domestic solar dryer for agricultural products. *INAE Lett.* **2019**, *4*, 147–160. [CrossRef]
12. Nabnean, S.; Nimnuan, P. Experimental performance of direct forced convection household solar dryer for drying banana. *Case Stud. Therm. Eng.* **2020**, *22*, 100787. [CrossRef]
13. Lingayat, A.; Chandramohan, V.; Raju, V. Design, development and performance of indirect type solar dryer for banana drying. *Energy Procedia* **2017**, *109*, 409–416. [CrossRef]
14. Sundari, A.U.; Neelamegam, P.; Subramanian, C. *An Experimental Study and Analysis on Solar Drying of Bitter Gourd Using an Evacuated Tube Air Collector in Thanjavur, Tamil Nadu, India*; Conference Papers in Science; Wiley Online Library: Hoboken, NJ, USA, 2013; p. 125628.
15. Mugi, V.R.; Chandramohan, V. Energy, exergy and economic analysis of an indirect type solar dryer using green chilli: A comparative assessment of forced and natural convection. *Therm. Sci. Eng. Prog.* **2021**, *24*, 100950. [CrossRef]

16. Bhardwaj, A.; Kumar, R.; Chauhan, R.; Kumar, S. Experimental investigation and performance evaluation of a novel solar dryer integrated with a combination of shs and pcm for drying chilli in the himalayan region. *Therm. Sci. Eng. Prog.* **2020**, *20*, 100713. [CrossRef]
17. Andharia, J.K.; Markam, B.; Dzhonova, D.; Maiti, S. A comparative performance analysis of sensible and latent heat based storage in a small-scale solar thermal dryer. *J. Energy Storage* **2022**, *45*, 103764. [CrossRef]
18. Shimpy; Kumar, M.; Kumar, A. Designs, performance and economic feasibility of domestic solar dryers. *Food Eng. Rev.* **2023**, *15*, 156–186. [CrossRef]
19. Rulazi, E.L.; Marwa, J.; Kichonge, B.; Kivevele, T. Development and Performance Evaluation of a Novel Solar Dryer Integrated with Thermal Energy Storage System for Drying of Agricultural Products. *ACS Omega* **2023**, *8*, 43304–43317. [CrossRef]
20. Sanghi, A.; Ambrose, R.P.K.; Maier, D. CFD Simulation of Corn Drying in a Natural Convection Solar Dryer. *Dry. Technol.* **2018**, *36*, 859–870. [CrossRef]
21. Simate, I.N. Simulation of the Mixed-Mode Natural Convection Solar Drying of Maize. *Dry. Technol.* **2001**, *19*, 1137–1155. [CrossRef]
22. Saniso, E.; Hayibaka, M. Fluid Dynamics (CFD) Simulation of a Solar Agricultural Dryer. *Int. J. Mech. Eng.* **2022**, *7*, 1230–1237.
23. Strelets, M. Detached Eddy Simulation of Massively Separated Flows. In Proceedings of the 39th Aerospace Sciences Meeting and Exhibit, Reno, NV, USA, 8–11 January 2001; p. 879.
24. Germano, M.; Piomelli, U.; Moin, P.; Cabot, W.H. A dynamic sub-grid scale eddy viscosity model. *Phys. Fluids* **1991**, *3*, 1760–1765. [CrossRef]
25. Rodriguez, S. RANS Turbulence Modeling. In *Applied Computational Fluid Dynamics and Turbulence Modeling: Practical Tools, Tips and Techniques*; Springer International Publishing: Berlin/Heidelberg, Germany, 2019; pp. 121–196.
26. Getahun, E.; Delele, M.A.; Gabbiye, N.; Fanta, S.W.; Demissie, P.; Vanierschot, M. Importance of integrated CFD and product quality modeling of solar dryers for fruits and vegetables: A review. *Sol. Energy* **2021**, *220*, 88–110. [CrossRef]
27. Rani, P.; Tripathy, M.A. CFD coupled heat and mass transfer simulation of pineapple drying process using mixed-mode solar dryers integrated with flat plate and finned collector. *Renew. Energy* **2023**, *217*, 119210. [CrossRef]
28. Behera, D.D.; Mohanty, R.C.; Mohanty, A.M. Thermal performance of a hybrid solar dryer through experimental and CFD investigation. *J. Food Process Eng.* **2023**, *46*, e14386. [CrossRef]
29. Aquilanti, A.; Tomassetti, S.; Muccioli, M.; Nicola, G.D. Design and experimental characterization of a solar cooker with a prismatic cooking chamber and adjustable panel reflectors. *Renew. Energy* **2023**, *202*, 405–418. [CrossRef]
30. Region, M. Civil Protection Service. Available online: http://84.38.48.145/sol/info.sol?lang=en (accessed on 21 November 2024).
31. Howell, J.R.; Siegel, R.; Menguc, M.P. *Thermal Radiation Heat Transfer*, 5th ed.; CRC Press: Boca Raton, FL, USA; Taylor&Francis Group: London, UK, 2011; p. 987.
32. Cheng, P. Two-Dimensional Radiating Gas Flow by a Moment Method. *AIAA J.* **1964**, *2*, 1662–1664. [CrossRef]
33. Bidi, M.; Hosseini, R.; Nobari, M.R.H. Numerical analysis of methane-air combustion considering radiation effect. *Energy Convers. Manag.* **2008**, *49*, 3634–3647. [CrossRef]
34. Kapulla, R.; Xiongguo, L.; Kelm, S.; Doll, U.; Paranjape, S.; Paladino, D. Importance, influence and limits of CFD radiation modeling for containment atmosphere simulations. *Nucl. Eng. Des.* **2023**, *411*, 112408. [CrossRef]
35. Chui, E.H.; Raithby, G.D. Computation of Radiant Heat Transfer on a Non-Orthogonal Mesh Using the Finite-Volume Method. *Numer. Heat Transf. Part B* **1993**, *23*, 269–288. [CrossRef]
36. Raithby, G.D.; Chui, E.H. A Finite-Volume Method for Predicting a Radiant Heat Transfer in Enclosures with Participating Media. *J. Heat Transf.* **1990**, *112*, 415–423. [CrossRef]
37. Issa, R.I.; Gosman, A.D.; Watkins, A.P. The computation of compressible and incompressible recirculating flows by a non-iterative implicit scheme. *J. Comput. Phys.* **1986**, *62*, 66–82. [CrossRef]